ARTICLES
https://doi.org/10.1038/s41563-019-0425-1
nature materials

Unjamming overcomes kinetic and proliferation arrest in terminally differentiated cells and promotes collective motility of carcinoma

Andrea Palamidessi[1,7], Chiara Malinverno[1,2,7*], Emanuela Frittoli[1,7], Salvatore Corallino[1], Elisa Barbieri[3], Sara Sigismund[2,3], Galina V. Beznoussenko[1], Emanuele Martini[1], Massimiliano Garre[1], Ines Ferrara[4], Claudio Tripodo[1,4], Flora Ascione[1], Elisabetta A. Cavalcanti-Adam[5], Qingsen Li[1], Pier Paolo Di Fiore[2,3], Dario Parazzoli[1], Fabio Giavazzi[6*], Roberto Cerbino[6*] and Giorgio Scita[1,2*]

During wound repair, branching morphogenesis and carcinoma dissemination, cellular rearrangements are fostered by a solid-to-liquid transition, known as unjamming. The biomolecular machinery behind unjamming and its pathophysiological relevance remain, however, unclear. Here, we study unjamming in a variety of normal and tumorigenic epithelial two-dimensional (2D) and 3D collectives. Biologically, the increased level of the small GTPase RAB5A sparks unjamming by promoting non-clathrin-dependent internalization of epidermal growth factor receptor that leads to hyperactivation of the kinase ERK1/2 and phosphorylation of the actin nucleator WAVE2. This cascade triggers collective motility effects with striking biophysical consequences. Specifically, unjamming in tumour spheroids is accompanied by persistent and coordinated rotations that progressively remodel the extracellular matrix, while simultaneously fluidizing cells at the periphery. This concurrent action results in collective invasion, supporting the concept that the endo-ERK1/2 pathway is a physicochemical switch to initiate collective invasion and dissemination of otherwise jammed carcinoma.

Collective motility is ruled by both biochemical and physical interactions that cells establish among each other and with their environment[1,2]. During tissue growth, cells are free to move, as in a fluid, but their motion becomes constrained as density increases. At a critical density—depending on a variety of biophysical parameters, such as intercellular adhesion, cortical tension, single-cell motility and cell shape variance—motility ceases and collectives rigidify, undergoing a jamming transition[3–7]. This transition ensures proper development of barrier properties in epithelial tissues, but also acts as a tumour-suppressive mechanism[3,8]. The reverse solid-to-liquid (unjamming) transition might, instead, represent a complementary gateway to epithelial cell migration, enabling mature tissues to flow[3,8,9]. However, how cells control the jamming and unjamming transitions is unclear.

Consistently with the emerging role of membrane trafficking in regulating cell migration plasticity and the mechanics of cell–cell interactions[10,11], we recently found that RAB5A, a master regulator of early endosomes necessary to promote a mesenchymal program of individual cancer invasion[12,13], impacts on the mechanics and dynamics of multicellular, normal and tumorigenic cell assemblies[14]. RAB5A overexpression reawakens the motility of otherwise kinetically arrested epithelial monolayers, promoting millimetre-scale, multicellular, ballistic cell locomotion and a flocking-fluid motility pattern through large-scale coordinated migration and local cell rearrangements[14–16]. Concurrently, monolayer stiffness, cell–cell surface contact and junctional tension increase, as well as the turnover of junctional E-cadherin and the extension of RAC1-driven protrusions[14]. Molecularly, impairing endocytosis, macropinocytosis or increasing fluid efflux abrogated RAB5A-induced collective motility, suggesting that perturbations of trafficking processes are necessary for the unjamming transition. However, the molecular nature of these endocytic-sensitive pathways is yet unidentified. Even less clear is whether this transition occurs in relevant physiological, 3D settings and whether it can promote collective dissemination of dense, jammed carcinoma.

Here, we identify a necessary axis of the flocking transition in a variety of jammed collectives. RAB5A overexpression enhances the internalization of the epidermal growth factor receptor (EGFR) through non-clathrin-dependent routes into endosomes, which causes hyperactivation of the extracellular signal-regulated protein kinases ERK1/2 and the phosphorylation of the branched actin nucleator, WAVE2[17]. This endocytic–ERK1/2 axis is sufficient to overcome the kinetic and proliferation arrest of mammary cysts in three dimensions. It also stimulates coherent rotation of breast ductal carcinoma in situ (DCIS) spheroid models, which causes both a radial gradient of cell fluidification and a stress-induced remodelling of the surrounding extracellular matrix (ECM). These effects combine to promote collective invasion of DCIS spheroids and ex vivo slices of orthotopically implanted DCIS, pointing at the identified RAB5A-mediated, epidermal growth factor (EGF)-dependent activation of endosomal ERK1/2 as a key molecular route to the unjamming-via-flocking transition. Pathologically, the identified

[1]IFOM, the FIRC Institute of Molecular Oncology, Milan, Italy. [2]University of Milan, Department of Oncology and Hemato-Oncology, Milan, Italy. [3]Istituto Europeo di Oncologia IRCCS, Milan, Italy. [4]Department of Health Sciences, Human Pathology Section, University of Palermo School of Medicine, Palermo, Italy. [5]Max Planck Institute for Medical Research, Heidelberg, Germany. [6]University of Milan, Department of Medical Biotechnology and Translational Medicine, Segrate, Italy. [7]These authors contributed equally: Andrea Palamidessi, Chiara Malinverno, Emanuela Frittoli. *e-mail: Chiara.Malinverno@ifom.eu; fabio.giavazzi@unimi.it; roberto.cerbino@unimi.it; Giorgio.Scita@ifom.eu

pathway appears relevant for breast carcinoma, RAB5A expression being upregulated in invasive foci of human DCIS and correlating with worse disease-free survival.

Results

EGFR trafficking controls flocking-liquid motility. RAB5A expression promotes a flocking transition in jammed, solid epithelial monolayers[14] through ill-defined molecular mechanisms and signalling axes. Particle image velocimetry (PIV) revealed that RAB5A expression enhanced cell motility, quantified by the root mean square velocity V_{RMS} (see Methods). It further promoted millimetre-scale coordination, measured by the velocity correlation length L_{corr}, and directed collective motion over a distance larger than ~700 µm, quantified by the persistence length L_{pers}, confirming previous results[14]. Removal of EGF, required for proliferation and single-cell motility of the MCF10A line[18], or addition of AG1478, an inhibitor of the EGFR kinase[19], abrogated RAB5A-induced flocking (Supplementary Videos 1, 2 and 4), with V_{RMS}, L_{corr} and L_{pers} reverting to values typical of control cells (Fig. 1a). These treatments further impacted on the uniformity of the migration pattern (Fig. 1b). We confirmed these results using EGFP-H2B-expressing cells to visualize nuclear cell displacements (Supplementary Video 3). Finally, similar EGF-dependency of collective motion was also observed in serum-starved, jammed keratinocyte monolayers, HaCat[20], and in oncogenically transformed MCF10A variants, MCF10.DCIS.com (Supplementary Fig. 8a and Supplementary Video 20).

Next, we tested whether alterations of endosomal biogenesis caused by RAB5A[21] perturbed EGFR cellular distribution, trafficking or signalling. Firstly, we showed that the total protein but not the messenger RNA (mRNA) levels of EGFR were significantly reduced following induction of RAB5A expression (Fig. 1c,d). The fraction of phosphorylated EGFR was, instead, unexpectedly increased (Fig. 1c). Secondly, RAB5A-expressing cells display a marked reduction of cell surface EGFR accompanied by increased intracellular EGFR, which accumulates in EEA1-positive, early endosomes (Fig. 1e–g). Measurements of the absolute number of surface EGFR using ^{125}I-EGF binding corroborated the immunofluorescence data (Fig. 1h). Finally, by immunofluorescence analysis (Supplementary Fig. 1a–c and Supplementary Table 1) and by determining the number of EGFR molecules on the plasma membrane (Supplementary Fig. 1d), we verified that the removal of the ligand and inhibition of EGFR kinase activity restore surface and intracellular distribution of EGFR to levels of control cells.

Intracellular accumulation of EGFR might originate from increased internalization or reduced recycling. In the former case, it is known that for a low EGF dose (1 ng ml^{-1}), EGFRs are primarily internalized by clathrin-mediated endocytosis[22] and recycled back to the plasma membrane[23]. For large physiological EGF concentrations (20–100 ng ml^{-1}), non-clathrin endocytosis[24] is activated in parallel to clathrin-mediated endocytosis[23,25]. RAB5A expression significantly increased the apparent endocytic rate constant (K_e) at high (30 ng ml^{-1}) but not at low (1 ng ml^{-1}) ^{125}I-EGF concentrations (Fig. 2a). We also measured the recycling rates of EGFR, which were not significantly altered by elevation of RAB5A (Fig. 2b), and the total levels of EGFR, which slowly, but progressively, decreased over time consistent with the augmented non-clathrin internalization that target EGFR to degradation (Supplementary Fig. 1e). To reinforce this finding, we measured EGFR internalization at high doses of ligands after silencing critical determinants of clathrin- and non-clathrin-endocytosis. We found that silencing dynamin-2 robustly reduced EGFR internalization by more than 80% in both control and RAB5A cells, consistent with the expected requirement of this protein for EGFR entry (Fig. 2c,d and Supplementary Table 2). The silencing of clathrin inhibited EGFR internalization to an extent similar to that achieved by dynamin-2 small interfering RNA (siRNA) in control cells, but was significantly less effective in RAB5A-expressing cells (Fig. 2c,d and Supplementary Table 2). Finally, the RAB5A-dependent increased rate of endocytosis was reduced to control levels after silencing of the endoplasmic reticulum (ER)-resident protein reticulon 3 (RTN3), essential for non-clathrin endocytosis[25] (Fig. 2c), or by impairing macropinocytosis using 5-(*N*-ethyl-*N*-isopropyl) amiloride (EIPA)[26] (Fig. 2e). Collectively, these findings indicate that RAB5A promotes EGFR non-clathrin endocytosis, leading to the accumulation of EGFR into early endosomes and, possibly, to the reawakening of collective motion. Indeed, silencing of dynamin-2 (Supplementary Fig. 2a,b and Supplementary Video 5), or RTN3, but not of its highly related ER resident protein RTN4 (Supplementary Fig. 2c,d and Supplementary Video 6), impaired RAB5A-induced flocking.

RAB5A activates ERK1/2 to regulate cell protrusion dynamics. EGFR signalling has been proposed to be initiated at the plasma membrane but to continue in endosomes[27–29], which act as signalling quanta-like platforms where phosphorylated EGFR can be packaged at constant mean amounts[30]. As a consequence, altering the size and number of endosomes directly affected EGFR signalling. Hence, we monitored EGFR downstream pathways following RAB5A expression.

We found no impact on phosphorylation levels of the two kinases AKT and p38, variably involved in motility, whereas phosphorylated ERK1/2 was increased (Fig. 3a) and long-lived in RAB5A-expressing cells (Supplementary Fig. 3a and Supplementary Table 3). We corroborated this finding by immunofluorescence after mixing control and EGFP-H2B-RAB5A-expressing cells (Supplementary Fig. 3b). Notably, ERK1/2 activation was detectable only in RAB5A-, but not in RAB5B- or RAB5C-expressing cells (Supplementary Fig. 3c,d). Only RAB5A increased significantly both the number and size distribution of EEA1-positive endosomes

Fig. 1 | Endocytic reawakening of motility is dependent on EGFR activation. a, PIV analysis of motion of control (CTR) and RAB5A-expressing-MCF10A monolayers in the presence or absence of EGF (Supplementary Videos 1 and 3) or the EGFR inhibitor AG1478 (Supplementary Video 2). Vertical lines indicate the time interval used for the analysis of motility parameters: V_{RMS}, root mean square velocity; C_{VV} velocity correlation functions as function of the distance r; L_{corr}, correlation lengths; MSD, mean square displacements obtained by numerical integration of the velocity maps over a given time interval, Δt; L_{pers}, persistence length. Data are from at least five videos/experimental conditions in four experiments. **b**, Snapshots of the velocity field obtained from PIV analysis of motion of control and RAB5A-MCF-10A monolayers treated as indicated (Supplementary Video 4). The colour map represents the alignment with respect to the mean instantaneous velocity, quantified by the parameter $a(x) = (\mathbf{v}(x) \cdot \mathbf{v}_0)/(|\mathbf{v}(x)||\mathbf{v}_0|)$. $a = 1(-1)$ when the local velocity is parallel (antiparallel) to the mean direction of migration. Scale bar, 100 µm. **c**, Immunoblot of the indicated proteins and quantification of total EGFR and phosphorylated/total EGFR value. Data are expressed relative to control after normalizing to vinculin (mean ± s.d., $n = 5$ independent experiments). M_w, molecular weight. **d**, Relative EGFR mRNA levels normalized to GAPDH (mean ± s.d., $n = 5$ independent experiments). **e**, Control and RAB5A-MCF10A cells were either permeabilized with 0.1% Triton X100 or not permeabilized before staining. Scale bar, 20 µm. **f**, Data are mean ± s.d. of total cell surface or internalized EGFR relative to control normalized to cell number ($n = 100$ cells in three independent experiments). **g**, Images of control and RAB5A-MCF10A monolayers stained with the indicated antibodies. Data are the mean ± s.d. of EEA1- and EGFR-positive vesicles/cells ($n > 150$ out of three independent experiments). Scale bar, 20 µm. **h**, Number of EGFRs per cell measured by ^{125}I-EGF saturation binding after subtracting unspecific background. Data are the mean ± s.d. of triplicate measurements. $^{**}p < 0.01$, $^{***}p < 0.001$, each-pair Student's *t*-test. n.s., not significant.

(Supplementary Fig. 3e–h and Supplementary Table 4), and significantly reduced surface EGFR levels, while augmenting the number of EGFR-positive structures (Supplementary Fig. 4a–e). RAB5B, instead, had marginal effects on endosome size and number, whereas RAB5C decreased significantly endosome number but robustly increased the size of EEA1- and EGFR-positive endosomes, which were concentrated perinuclearly (Supplementary Figs. 3e–h and 4a–e). RAB5B and RAB5C were also very inefficient in reawakening collective motion in jammed monolayers (Supplementary Fig. 4f and Supplementary Video 7). Additionally, pharmacological inhibition of ERK1/2 using PD0325901 that targets the upstream MEK kinase[31], or SCH772984 that directly inhibits ERK1/2 activity, abrogated RAB5A-induced flocking (Fig. 3b and Supplementary Video 8). Treatment with AG1478 or dynasore, a small molecule impairing dynamin-2 activity[32], inhibited RAB5A-mediated elevation of ERK1/2 (Fig. 3c) and blocked the reawakening of collective

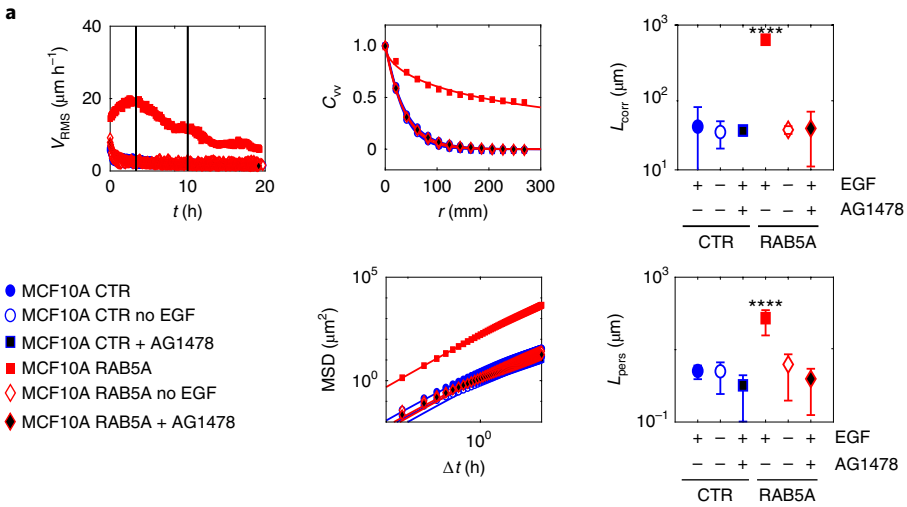

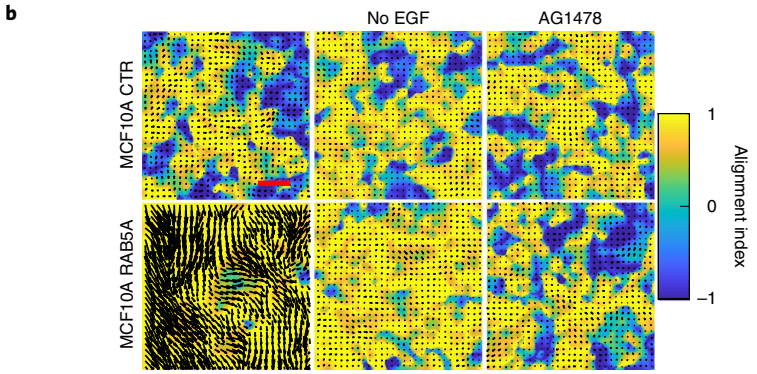

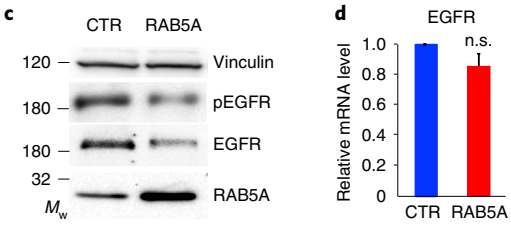

	EGFR	pEGFR/EGFR
CTR	1	1
RAB5A	0.39 ± 0.19	***1.8 ± 0.31

***$P < 0.001$

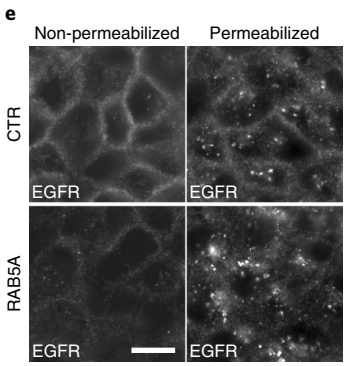

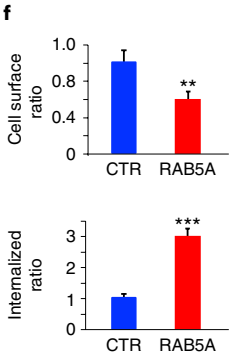

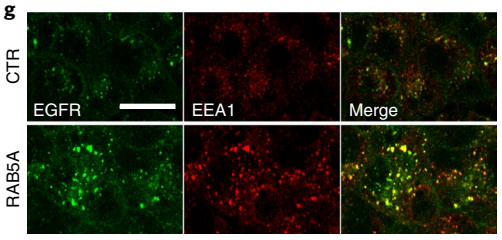

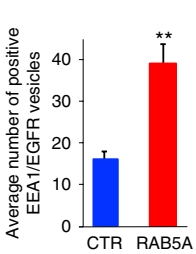

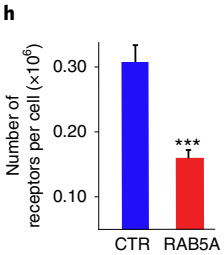

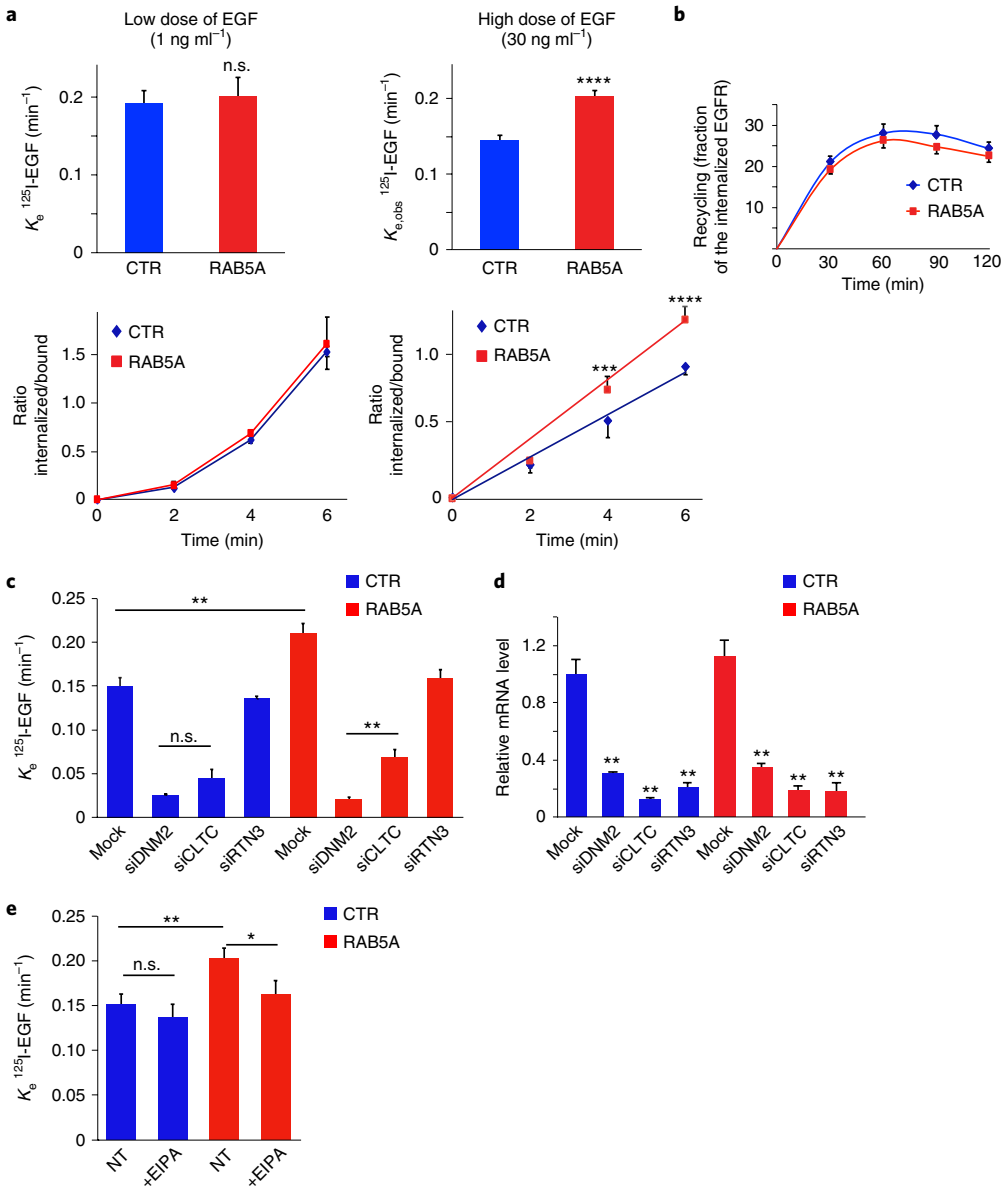

Fig. 2 | RAB5A increases non-clathrin internalization of EGFR. a, Effective or apparent internalization rate constants at low (1 ng ml^{-1}) or high (30 ng ml^{-1}) concentrations of ^{125}I-EGF, respectively (K_e, upper panel), in control and RAB5A-expressing monolayers. A representative kinetic of the ratio of ^{125}I-EGF internalized/bound is shown (bottom panels) and is expressed as the mean ± s.d. ($n = 3$ out of 12 independent experiments). ****$p < 0.0001$. *P* values, each-pair Student's *t*-test. **b**, Control and RAB5A-MCF10A cell monolayers were incubated with ^{125}I-EGF (30 ng ml^{-1}) for 15 min at 37 °C. Recycling of ^{125}I-EGF at the indicated time points was estimated as described in the Methods. Data are the mean ± s.d. ($n = 3$ replicates in a representative experiment). **c**, EGFR internalization kinetics in control and RAB5A-expressing monolayers silenced for dynamin-2 (DNM2), clathrin heavy chain (CLTC) or reticulon 3 (RTN3) using ^{125}I-EGF at high (30 ng ml^{-1}) concentrations. Results are the mean ± s.d. ($n = 3$ independent experiments) of the apparent internalization rate constants, K_e. **$p < 0.01$. *P* values, each-pair Student's *t*-test (the comparison between paired values is indicated). See Supplementary Table 2 for additional statistics. **d**, The effectiveness of silencing was measured by qRT-PCR. Data are expressed relative to control after normalizing to GAPDH. The data are the relative level of gene expression compared to control expressed as mean ± s.d. ($n = 3$ independent experiments). **$p < 0.01$, *P* values, each-pair Student's *t*-test (siRNA versus control). **e**, EGFR internalization kinetics in control and RAB5A-expressing cell monolayers treated with vehicle or 5-(*N*-ethyl-*N*-isopropyl) amiloride (EIPA) (75 μM) were measured using ^{125}I-EGF at high (30 ng ml^{-1}) concentration. Results are mean ± s.d. ($n = 3$ independent experiments) of the apparent internalization rate constants, K_e. *$p < 0.05$, **$p < 0.01$. *P* values, each-pair Student's *t*-test (the comparison between each paired value is indicated). NT, not treated; n.s., not significant.

motion (Fig. 1, Supplementary Videos 2 and 9, and ref. [14]), suggesting that RAB5A elevation might enhance endosomal ERK1/2 signalling. This conjecture was tested by generating a Förster resonance energy transfer (FRET) EKAREV-ERK1/2 sensor[33], targeted to the endosomes by appending the FYVE domain of SARA protein to its C-terminus[34] (Supplementary Fig. 4g,h). Removal of EGF or treatment with PD0325901 significantly impaired FRET efficiency, validating the biological relevance of the sensor (Supplementary Fig. 4i). More importantly, RAB5A-expressing cells displayed increased endosomal ERK1/2 FRET efficiency as compared with control monolayers (Supplementary Fig. 4j). We further showed that global elevation of ERK1/2 phosphorylation induced by the expression of

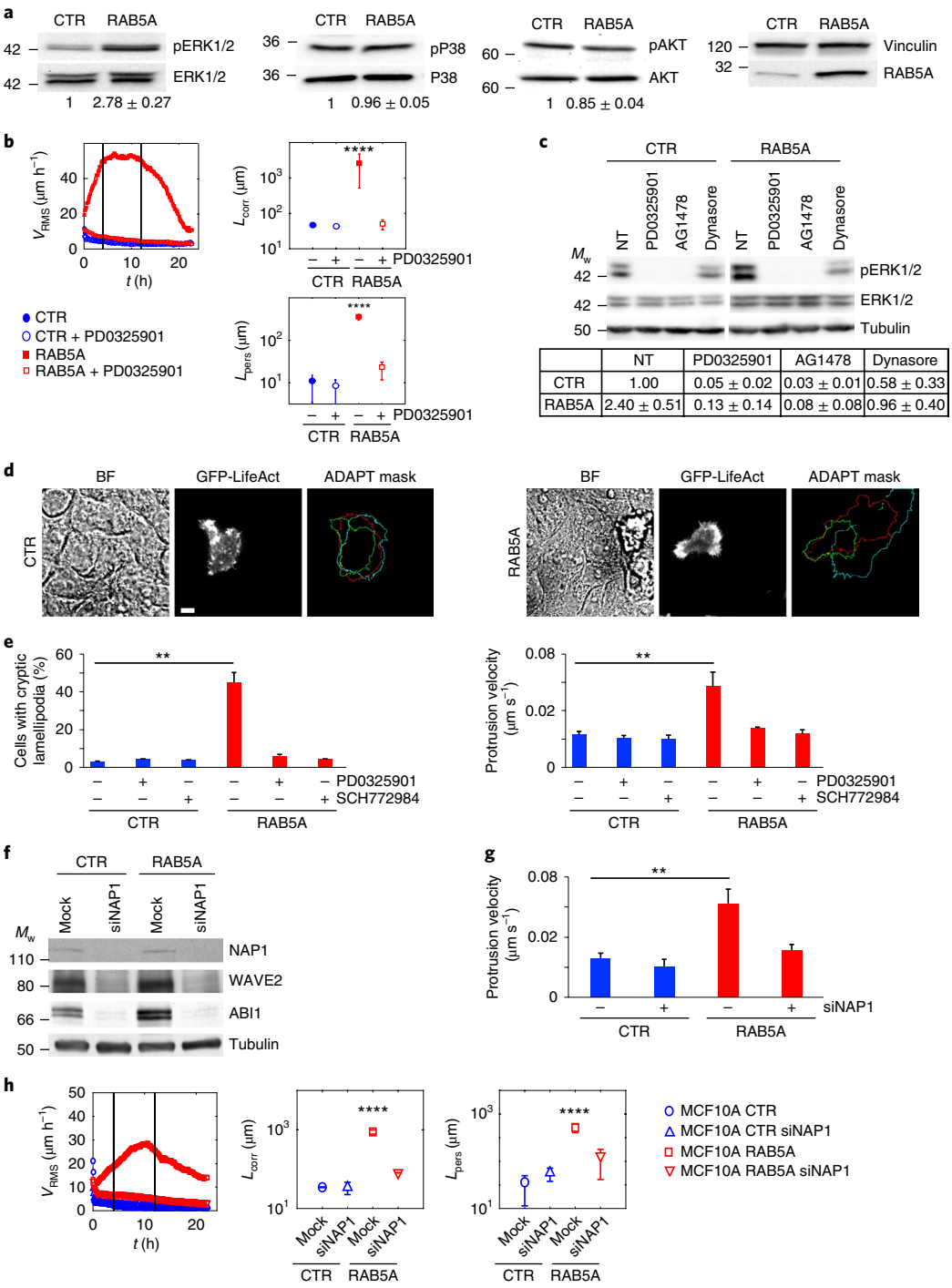

	NT	PD0325901	AG1478	Dynasore
CTR	1.00	0.05 ± 0.02	0.03 ± 0.01	0.58 ± 0.33
RAB5A	2.40 ± 0.51	0.13 ± 0.14	0.08 ± 0.08	0.96 ± 0.40

Fig. 3 | RAB5A endosomal ERK1/2 activity is required for flocking locomotion. a, Immunoblot of control and RAB5A-MCF10A monolayers with the indicated antibodies. The ratio of phosphorylated/total levels of the indicated proteins is expressed as the mean ± s.d. ($n = 5$ independent experiments). **b**, PIV analysis of motion (Supplementary Video 8) of control and RAB5A-MCF10A monolayers treated with vehicle or PD0325901 (1 μM), a MEK inhibitor, to extract V_{RMS}, L_{corr} and L_{pers}. Data are the mean ± s.d. ($n = 5$ videos/conditions out of three independent experiments). **c**, Immunoblot of control and RAB5A-MCF10A monolayers treated with PD0325901, AG1478 or dynasore (80 μM), or vehicle as control with the indicated antibodies. The ratio of phosphoERK1/2/totalERK1/2 is expressed as the mean ± s.d. ($n = 4$ independent experiments). **d**,**e**, Still phase-contrast and fluorescent images of cryptic lamellipodia in control and RAB5A-MCF10A monolayers composed of mosaically GFP-LifeAct-expressing (green):non-expressing cells (1:10 ratio) from Supplementary Video 11. Examples of the fluctuation of cell contours at 0 min (green), 45 min (red) and 90 min (blue) in the ADAPT mask image. Scale bars, 20 μm. BF, bright-field. In **e**, the number of cells with lamellipodium and velocity of protrusion fluctuations are expressed as mean ± s.d. ($n = 65$ cells/conditions from four independent experiments). **f**, Immunoblotting of control and RAB5A-MCF10A cell monolayers silenced for the critical WAVE complex component, NAP1. **g**, Analysis of the dynamics of cell protrusions of mosaically expressing GFP-LifeAct, control and RAB5A-MCF10A monolayers silenced for NAP1 (Supplementary Video 12). The velocity of protrusion fluctuations is the mean ± s.d. ($n = 96$ cells/conditions from three independent experiments). **h**, PIV analysis of motion (Supplementary Video 13) of control and RAB5A-MCF10A monolayers silenced for NAP1 to extract V_{RMS}, L_{corr} and L_{pers}. Data are the mean ± s.d. ($n = 5$ videos/conditions out of three independent experiments). $^{**}p < 0.01$, $^{****}p < 0.0001$, P values, each-pair Student's t-test.

a constitutively activated MEK-DD did not reawaken motility in jammed monolayers (Supplementary Fig. 5a,b and Supplementary Video 10). Notably, MEK-DD had no impact on junctional straightness or morphology (Supplementary Fig. 5c,d). Collectively, our findings indicate that ERK1/2 activation is necessary, albeit not sufficient, to promote unjamming.

RAB5A-expressing, unjammed monolayers move in a directed fashion by extending oriented cryptic lamellipodia[14,35] (Fig. 3d). Cryptic lamellipodia depend on RAC1, which activates branched actin polymerization of the pentameric WAVE2 complex[36]. The key component of this complex, WAVE2 is phosphorylated by ERK1/2 on multiple serine residues, among which S343 and S351, to be activated and to control protrusion dynamics[37]. Consistently, we found that RAB5A expression increased the phosphorylation of WAVE2, but marginally of ABI1, another key component of the WAVE complex[36], in an ERK1/2-, EGFR- and dynamin-2-dependent manner (Supplementary Fig. 6a–c). Additionally, by monitoring the dynamics of cells mosaically expressing EGFP-LifeAct, we found that pharmacological inhibition of ERK1/2 impaired the formation and dynamics of cryptic lamellipodia (Fig. 3d,e and Supplementary Video 11). Similar results were obtained by silencing of NAP1, a critical member of the complex. This treatment destabilized both WAVE2 and ABI1 proteins (Fig. 3f), as previously shown[38,39], impaired cryptic lamellipodia dynamics (Fig. 3g and Supplementary Video 12), flocking (Fig. 3h and Supplementary Video 13) and wound closure (Supplementary Fig. 6d–f and Supplementary Video 14). Silencing of only WAVE2 in MCF10A cells, which also express WAVE1 and WAVE3 mRNA (Supplementary Fig. 6g), was, as expected, less effective (Supplementary Fig. 6d,e and Supplementary Video 14).

Unjamming terminally differentiated mammary acini. To explore the biological consequences of the RAB5A-induced endo-ERK1/2 axis, we exploited the ability of MCF10A cells to generate differentiated, kinetically and proliferation-arrested hollow cysts grown over Matrigel plugs[18] (Supplementary Fig. 7a). We employed mCherry-H2B-expressing control and RAB5A cells to monitor the kinematics of differentiated cysts (Fig. 4a). Cells in control differentiated acini were kinetically arrested, whereas expression of RAB5A reawakened motility by triggering rotational motion (Fig. 4b,c and Supplementary Video 15). With custom PIV, we quantified the tangential rotational velocity field and extracted relevant kinematic parameters, such as V_{RMS} and the rotational order parameter ψ, which can vary between 0 (absence of coordinated motion) and 1 (for a rigidly rotating sphere) (see Methods). Control acini displayed barely detectable V_{RMS}, with ψ below 0.2 (Fig. 4c and Supplementary Videos 15 and 16), whereas following RAB5A expression ψ reached a value close to 1 in correspondence to the maximum of V_{RMS} (Fig. 4c and Supplementary Videos 15 and 16).

Impaired EGFR activity, ERK1/2 phosphorylation and dynamin endocytosis reduced V_{RMS} and ψ to control levels (Fig. 4d and Supplementary Video 17). Additionally, RAB5A cysts displayed elevated phospho-ERK1/2 (Supplementary Fig. 7b) and straight and compact junctions (Supplementary Fig. 7c), indicating that RAB5A impacts on similar biochemical and microscopic determinants as in 2D monolayers[14].

We also noticed that inducing RAB5A expression in the initial phase of cystogenesis reduced the number of acini, but the ones remaining were significantly larger (Fig. 4e,f), and did not undergo proliferation arrest, like control cysts do, as revealed by Ki67 staining, or apoptosis (Supplementary Fig. 7d). Importantly, proliferation was not a prerequisite for motility, since treatment with Mitomycin C had no effects on rotations (Supplementary Video 18). We investigated this phenotype further by inducing RAB5A expression at the end of morphogenesis, when fully differentiated acini have ceased proliferation and motility[18]. RAB5A expression reawakened not only cell motility (Supplementary Video 19), but also proliferation in an ERK1/2-dependent manner (Fig. 4g,h).

The ERK1/2-dependent reawakening of collective motion and proliferation of terminally differentiated acini has been associated with the initiation of a more complex program of branched morphogenesis that begins with the formation of multicellular buds[40]. This process requires in addition to specific growth factors, also cell interaction with the microenvironment and ECM components[41,42]. Collagen type-I, for example, has been used to increase chemomechanical signalling and facilitate duct morphogenesis[43]. Henceforth, we grew MCF10A cells over mixed Matrigel–collagen gels[42]. Under these conditions, RAB5A expression caused cysts to lose their spherical roundness, and promoted the formation of buds (Fig. 4i,j).

Endocytic unjamming promotes carcinoma collective invasion. To determine whether RAB5A unjamming can be exploited by breast cancer lines to enhance collective motility and invasiveness, we employed MCF10.DCIS.com cells, which are isogenic to MCF10A cells, express oncogenic T24-H-RAS and are used as models for the progression of DCIS to invasive carcinoma[44]. During the DCIS phase, cells grow under intraductal confinement where cell packing and density exert mechanical stress and supress tumour motility and progression. Consistently, MCF10.DCIS.com cells plated as confluent monolayers are kinetically arrested. RAB5A expression promoted the reawakening of collective motion[14] (Supplementary Fig. 8a and Supplementary Video 20) and accelerated wound closure of monolayers, which instead of arresting after the opposing fronts collided kept on flowing, reminiscent of 'a wound that never heals'[45] (Fig. 5a–c and Supplementary Video 21). Biochemically, RAB5A expression decreased total EGFR levels, but increased ERK1/2 without affecting AKT or p38 phosphorylation (Supplementary Fig. 8b). Next, we monitored the kinematics of mCherry-H2B control and RAB5A-expressing MCF10.DCIS.com spheroids embedded into native collagen type-I by developing 3D differential variance analysis (see Methods). Whereas control cells displayed as low,

Fig. 4 | RAB5A overcomes kinetic and proliferation arrest in terminally differentiated acini. a–c, Single *Z* planes from Supplementary Video 15 of control and RAB5A-MCF10A-expressing mCherry-H2B acini. RAB5A mRNA levels relative to control after normalizing to GAPDH are shown as mean ± s.d. ($n = 3$ independent experiments). Scale bar, 50 μm. **b**, Tangential velocity fields at $t = 10$ h (yellow arrows) from PIV analysis, overlaid on radial projections of acini onto a unit spherical surface (Supplementary Video 16). The red arrow is parallel to the instantaneous total angular momentum **l** and provides the orientation of the instantaneous axis of rotation. Its length is equal to the instantaneous order parameter ψ. **c**, Time evolution of V_{RMS} and ψ (see main text and Methods) representative of four videos in three experiments. **d**, V_{RMS} and ψ calculated over the 4–12 h (Supplementary Video 17) time window for control and RAB5A-MCF10A mCherry-H2B-expressing MCF10A acini treated as indicated. Average values are from 5 movies in 3 independent experiments. **e**, Control and RAB5A-MCF10A acini treated as indicated above were processed for phase-contrast imaging to monitor acini shape and size. Scale bar, 100 μm. **f**, Acini size expressed as the mean ± s.d. ($n = 100$ acini/conditions in five independent experiments). **g**, Immunofluorescence images of control and RAB5A-MCF10A acini treated with doxycycline as indicated in the presence or absence of PD0325901. Scale bar, 80 μm. **h**, Acini diameter and the number of KI67-positive cells/total number of cells per acini is reported as mean ± s.d. ($n = 25$ acini/conditions in three independent experiments). **i**, Control and RAB5A-MCF10A acini grown on mixed 1:1 Matrigel:collagen type-I plugs for 21 days were processed for phase-contrast imaging. Scale bar, 100 μm. **j**, Acini area and roundness is expressed as mean ± s.d. ($n = 40$ acini/conditions in five experiments). $^{*}p < 0.05$, $^{**}p < 0.01$. *P* values, each-pair Student's *t*-test.

uncorrelated, disordered motion (Fig. 5d,e, Supplementary Fig. 8c and Supplementary Video 22), RAB5A-MCF10.DCIS.com cells acquired collective rotational motility, characterized by a large angular velocity Ω (of the order of ~12 rad h^{-1}) and a strong orientational persistence of the instantaneous axis of rotation, captured by the decay time of the orientational correlation function (Fig. 5e and Supplementary Fig. 8c). We also observed a speed-up of the local cell rearrangement dynamics, estimated by calculating the overlap

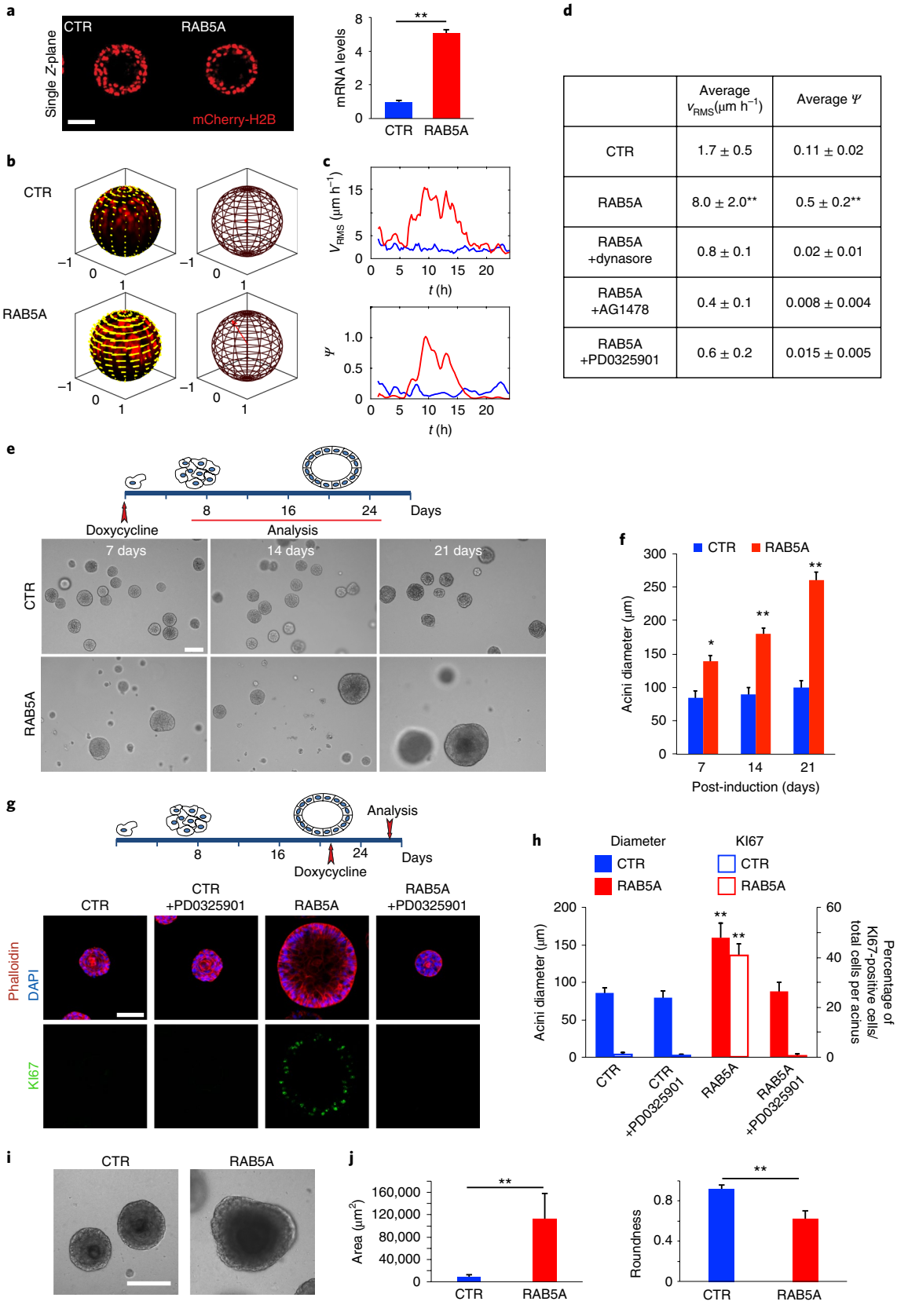

	Average v_{RMS}(μm h^{-1})	Average Ψ
CTR	1.7 ± 0.5	0.11 ± 0.02
RAB5A	8.0 ± 2.0**	0.5 ± 0.2**
RAB5A +dynasore	0.8 ± 0.1	0.02 ± 0.01
RAB5A +AG1478	0.4 ± 0.1	0.008 ± 0.004
RAB5A +PD0325901	0.6 ± 0.2	0.015 ± 0.005

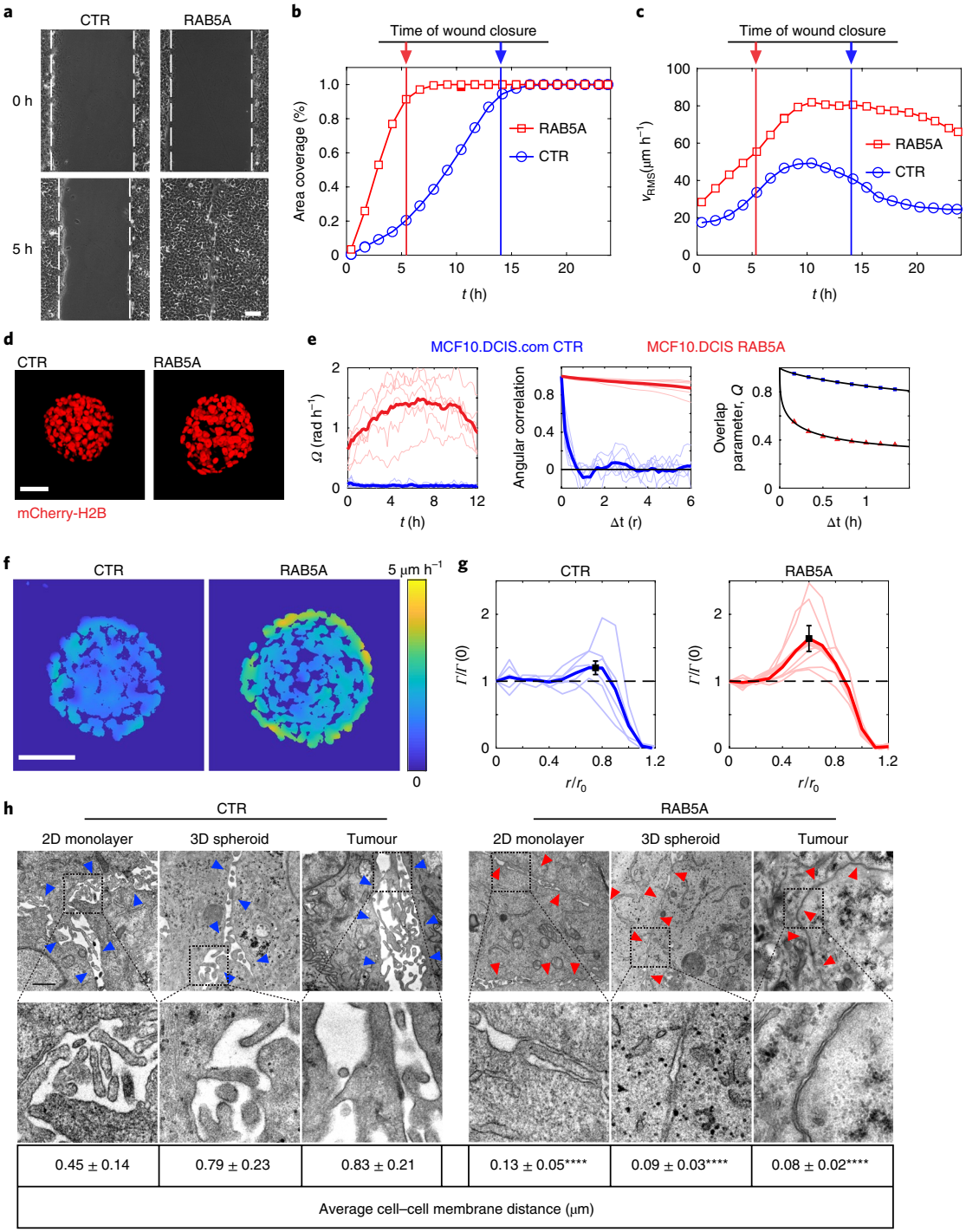

Fig. 5 | RAB5A promotes the emergence of coordinated angular rotation in cancer spheroids. a–**c**, Stills of scratched wound migration in control and RAB5A-MCF10.DCIS.com monolayers. Dashed lines mark the wound edges. Scale bar, 100 μm. **b**,**c**, Motility (Supplementary Video 21) was quantified as the percentage of area covered (**b**) or V_{RMS} (**c**). Vertical bars indicate the time at which wounds closed. Data are representative of 1 experiment out of >10. **d**, Snapshots of mCherry-H2B-expressing, control and RAB5A-MCF10.DCIS.com spheroids embedded in collagen type-I (6.0 mg ml^{-1}). Scale bar, 100 μm. **e**, Image differential variance-based analysis (3D DVA) of 5–8 spheroid/conditions in three independent experiments (Methods and Supplementary Video 22) was performed to extract the angular velocity Ω (rad h^{-1}), the angular correlation of motion quantified by considering the decay of the orientational correlation function, and the overlap parameter Q captured from the non-rigid part of motion, involving mutual cell rearrangement and fluid-like dynamics. **f**,**g**, Maps of the RMS velocity fluctuations on the equatorial plane of a CTR and RAB5A-expressing spheroid. Scale bar, 100 μm. In **g**, azimuthally averaged radial profiles of the relaxation rate Γ, for CTR and RAB5A spheroids, obtained with 3D DVA analysis (Supplementary Video 23). Curves are scaled along the x axis with the radius r_0 of each spheroid and along the y axis with the value of the relaxation rate $\Gamma(0)$ at the centre of spheroid. Thick curves represent the average value with peaks at 1.2 ± 0.1 and 1.6 ± 0.2 (n = 7 for each condition). $p < 0.05$, each-paired Student's t-test. The black data points indicate the peak values ±s.d. **h**, Electron microscopy of control and RAB5A-MCF10.DCIS.com monolayers, 3D spheroids or tumour orthotopically injected into immune-compromised mice. Blue arrows point to cell–cell contact spaces, red arrows to tight cell–cell contacts. Scale bar, 2 μm. The average distance between adjacent cells is reported below as mean ± s.d. (n = 35 cell–cell junctions in random fields in three experiments). ****$p < 0.001$. P values, each-pair Student's t-test.

parameter $Q(\Delta t)$, which quantifies (see Methods) the fraction of nuclei that have been displaced from their original position during a time interval of duration (Δt) when observed in a reference frame co-moving with the whole spheroid (Fig. 5e and Supplementary Fig. 8c). The decay of $Q(\Delta t)$ does not depend on the rigid motion of the spheroid as a whole, but captures, instead, the 'fluid-like' relative motion of cells.

By repeating the same analysis in a space-resolved fashion (see Methods), we discovered that, for RAB5A-MCF10.DCIS.com spheroids, the decorrelation rate associated with the decay of the local overlap parameter displayed a systematic radial dependence, being much larger at the periphery of the spheroid (Fig. 5f,g). The presence of a 'melted' layer of cells on the surface of the rotating spheroid was confirmed by an optical-flow analysis (see Methods) of the velocity fluctuations (Supplementary Video 23) that, after removal of the global rotation, exhibited a marked increase close to the boundaries (Fig. 5f,g).

Endocytic-mediated liquid-like collective rotation in RAB5A-MCF10.DCIS.com spheroids was dependent on EGFR activity, ERK1/2 phosphorylation and dynamin-2 and abrogated by inhibiting ARP2/3-mediated actin polymerization (Supplementary Fig. 8c and Supplementary Video 24). Furthermore, electron microscopy morphological analysis of monolayers, spheroids and orthotopically injected tumours revealed that RAB5A expression induces junctional straightening and increases cell–cell contact area (Fig. 5h). Thus, similar cellular/biochemical processes driving 2D locomotion and acini morphogenesis control the dynamics of oncogenic epithelial ensembles.

Next, we explored the consequence of endocytic-mediated unjamming by monitoring oncogenic spheroids co-expressing EGFP-LifeAct and mCherry-H2B over longer timescales. Invariably, RAB5A promoted collective angular motion and the formation of invasive, multicellular buds and strands, suggesting that unjamming and collective invasion might be temporally coordinated and possibly coupled (Fig. 6a,b and Supplementary Video 25).

Collective invasion into native collagen type-I, which, at the concentration used, forms a dense fibrillar network (Supplementary Fig. 8d), can only occur following its remodelling. To verify this, we exploited fluorescent functionalized-beads that bind to the collagen fibres, impeding relative motion between beads and the ECM used to embed the spheroids (Fig. 6c and Supplementary Video 26). We developed stress fluctuation microscopy (see Methods) to infer, from the instantaneous velocity maps of the tracers (Supplementary Video 27), an estimate of the root mean square (RMS) values of the fluctuating strains induced by the cellular motion onto the ECM. Reconstructed normal RMS stresses are obtained (Fig. 6d,e and Supplementary Video 27) via the constitutive equations of the material, whose Young's modulus $E = 135 \pm 57$ Pa was measured using atomic force microscopy (Supplementary Fig. 8d). The RMS stresses imposed on the matrix by RAB5A spheroids were about two times larger than controls (Fig. 6e). The corresponding RMS normal strain at the boundary of RAB5A-expressing cells was of the order of about 10%, well above the critical value (strain ~5–6.5%) at which native collagen gels start exhibiting a nonlinear mechanical response and strain-induced remodelling[46–48]. Consistently, RAB5A-expressing rotating spheroids extensively remodelled fibrillary collagen, detected by second-harmonic generation signals of two-photon illumination, generating gaps and channels (Supplementary Fig. 8e). EGFR, ERK1/2, dynasore and ARP2/3 inhibitor of collective angular motion also prevented collagen remodelling and invasion (Fig. 6f).

Next, we extended this finding using ex vivo organotypic tumour slices from mCherry-H2B- and EGFP-LifeAct-expressing DCIS orthotopically injected into immunocompromised mice. Tumour masses were mechanically excised and grown as organotypic tissue slices at the air/liquid interface (see Methods and ref. [49]). Whereas control tumours were immobile, jammed and compacted, RAB5A-expressing malignant cells became highly motile and appeared to stream like a flowing liquid (Supplementary Video 28), also captured by PIV (Fig. 6g,h and Supplementary Video 29). Thus, endocytic unjamming of kinetically arrested DCIS tumours is sufficient to instigate motility and promote collective invasion.

The pathophysiological relevance of our findings is underscored by the observations that RAB5A is deregulated in breast cancer[13,50], and specifically during the invasive progression of human ductal breast carcinomas. Indeed, RAB5A expression was low in malignant cells of densely packed and jammed DCIS foci. The percentage of strongly expressing RAB5A cells increased at foci of DCIS associated with invasive components or in overt infiltrating carcinomas (IDC) (Supplementary Fig. 9a). Additionally, increased RAB5A expression was detected in aggressive breast cancer cell lines (Supplementary Fig. 9b), and correlated with worse relapse-free probability in various breast cancer subtypes (Supplementary Fig. 9c).

Conclusions

We identify a molecular route that reinstates multicellular rearrangements in otherwise immobile mature epithelia and densely packed carcinoma. Biochemically we showed that elevated RAB5A enhances non-clathrin endocytosis of EGFR and promotes its accumulation in to endosomal vesicles, which become signalling platforms for the prolonged and elevated activation of ERK1/2. This, in turn, is sufficient to promote the hyperphosphorylation of WAVE2 that, by controlling actin polymerization, contributes to the extension of oriented, cryptic lamellipodia[35]. Physically, the latter protrusions exert increased traction forces[14,51], and enhance cell

Fig. 6 | RAB5A promotes collective invasion in tumour spheroids and tumour slices. a,**b**, Invasive structures in EGFP-LifeAct and mCherry-H2B-co-expressing control and RAB5A-MCF10.DCIS.com spheroids embedded in collagen type-I (Supplementary Video 25). The line delineates an invasive multicellular bud; the arrow points to an invasive strand. The percentage of spheroids with invasive structures is expressed as the mean ± s.d. ($n = 15$/experimental conditions in five independent experiments). $^{**}p < 0.01$, each-paired Student's t-test. Scale bar, 150 μm. **c**, Snapshots (Supplementary Video 26) of mCherry-H2B-expressing control and RAB5A-MCF10.DCIS.com spheroids embedded in collagen type-I interspersed with functionalized fluorescent beads (Fluobeads). Scale bar, 200 μm. **d**, Maps of RMS normal stresses on the ECM in the equatorial plane of CTR and RAB5A-expressing spheroids (Supplementary Video 27). **e**, Azimuthally averaged radial profiles of the RMS normal stress σ and of the RMS normal strain ε for CTR and RAB5A spheroids. Curves are scaled along the x axis with the radius r_0 of each spheroid. Thick curves are the average of analysed spheroids. The shaded region corresponds to the critical strain above which collagen undergoes strain-induced structural remodelling and nonlinear mechanical response[46]. $p < 0.01$, pair Student's t-test. **f**, Second-harmonic generation analysis of collagen type-I fibres used to embed mCherry-H2B-expressing control and RAB5A-MCF10.DCIS.com spheroids in the presence of vehicle or the indicated inhibitors. The percentage of spheroids with invasive structures is expressed as the mean ± s.d. ($n = 15$/experimental conditions in five independent experiments). $^{**}p < 0.01$, each-pair Student's t-test. Scale bar, 70 μm. **g**,**h**, Experimental scheme. EGFP-LifeAct and mCherry-H2B-expressing control and RAB5A-MCF10.DCIS.com DCIS orthotopically injected into immunocompromised mice were mechanically excised and placed at the air/liquid interface, and monitored by time-lapse microscopy (Supplementary Video 28). PIV analysis to extract the cellular V_{RMS} (Supplementary Video 29). Boxed areas indicate fields of view for the analysis (at least 5 fields of view/movie for three independent experiments). Scale bar, 150 μm. In **h**, thick lines are averages of the time-dependent V_{RMS} for each field of view (thin lines) in CTR and RAB5A tumours.

orientation, promoting flocking in epithelia monolayers and long-range coordinated rotation in 3D cysts and spheroids.

Remarkably, RAB5A-expressing spheroids display a radial gradient of fluidity whereby cells at the periphery in contact with the ECM exhibit faster rearrangement dynamics and increased tissue fluidization. These kinematic changes are linked to increased strains and/or stresses exerted on the surrounding ECM beyond the threshold for remodelling fibrillar collagen[46], thereby facilitating the generation of tracks and channels into which fluidized cells advance collectively. These mechanical changes are remarkably reminiscent of the graded unjamming (solid-to-fluid) transition observed along the body axis of developing zebrafish embryo and shown to drive body axis elongation[52]. They further point to the concept that spatiotemporal control of fluid-like and solid-like tissue states, and

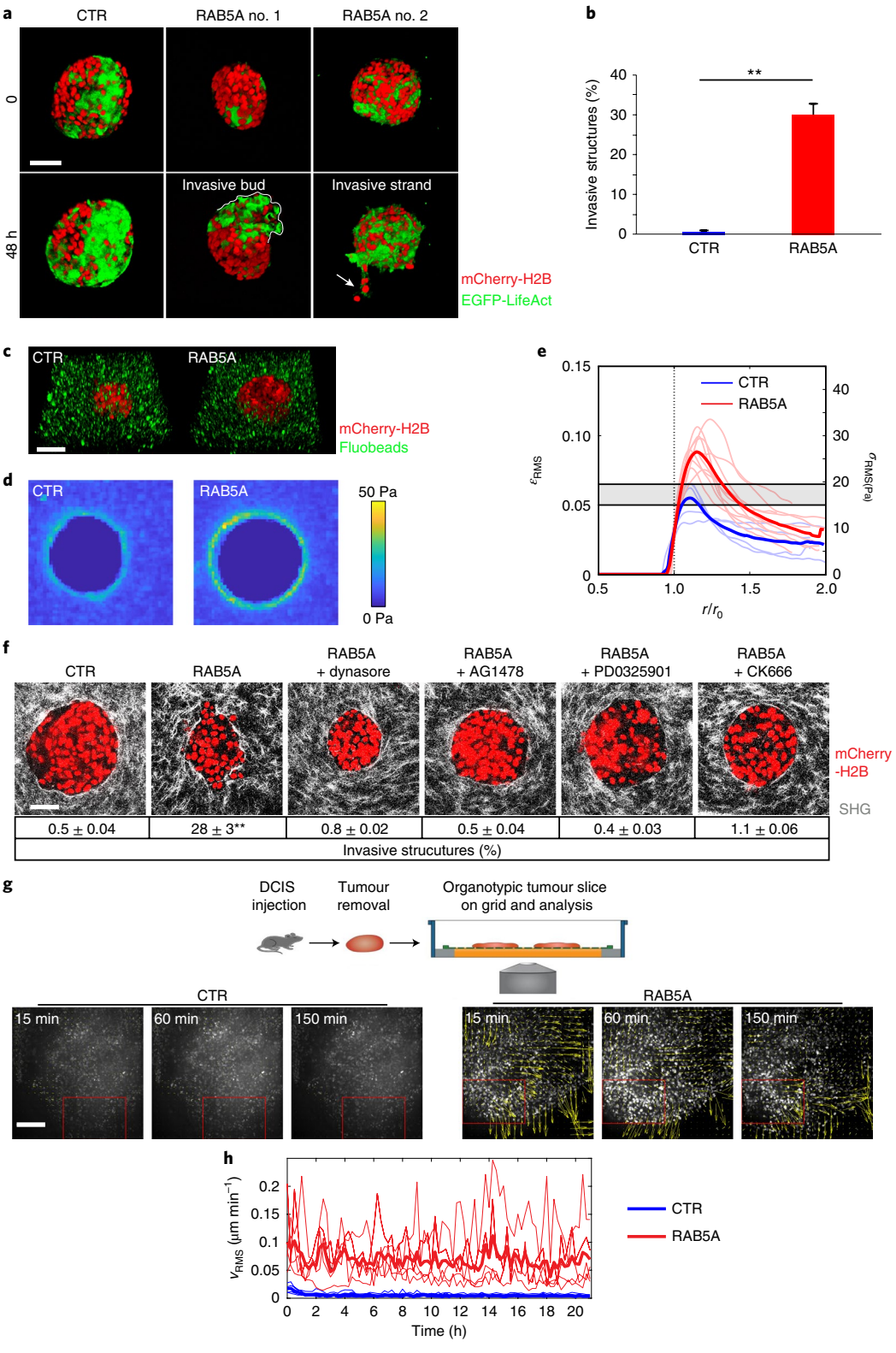

graded fluidization specifically, might be a general physical mechanism of diverse multicellular collectives. This mechanism might emerge as an adaptive 'smart material' strategy of cell collectives in response to variations in the chemical/mechanical composition of the ECM and might further impact on the structural composition of the surrounding stroma. Within this context, the transition from DCIS, which grow under intraductal confinement where extreme cell packing and density exert mechanical stress and supress motility, to invasive carcinoma, which disperse locally also through collective invasion[53], represents a case in point.

Online content

Any methods, additional references, Nature Research reporting summaries, source data, statements of code and data availability and associated accession codes are available at https://doi.org/10.1038/s41563-019-0425-1.

Received: 22 August 2018; Accepted: 5 June 2019;
Published online: 22 July 2019

References

1. Hakim, V. & Silberzan, P. Collective cell migration: a physics perspective. *Rep. Prog. Phys.* **80**, 076601 (2017).
2. Haeger, A., Wolf, K., Zegers, M. M. & Friedl, P. Collective cell migration: guidance principles and hierarchies. *Trends Cell Biol.* **25**, 556–566 (2015).
3. Park, J. A., Atia, L., Mitchel, J. A., Fredberg, J. J. & Butler, J. P. Collective migration and cell jamming in asthma, cancer and development. *J. Cell Sci.* **129**, 3375–3383 (2016).
4. Bi, D., Yang, X., Marchetti, M. C. & Manning, M. L. Motility-driven glass and jamming transitions in biological tissues. *Phys. Rev. X* **6**, 021011 (2016).
5. Sadati, M., Taheri Qazvini, N., Krishnan, R., Park, C. Y. & Fredberg, J. J. Collective migration and cell jamming. *Differentiation* **86**, 121–125 (2013).
6. Atia, L. et al. Geometric constraints during epithelial jamming. *Nat. Phys.* **14**, 613–620 (2018).
7. Garcia, S. et al. Physics of active jamming during collective cellular motion in a monolayer. *Proc. Natl Acad. Sci. USA* **112**, 15314–15319 (2015).
8. Oswald, L., Grosser, S., Smith, D. M. & Kas, J. A. Jamming transitions in cancer. *J. Phys. D* **50**, 483001 (2017).
9. Haeger, A., Krause, M., Wolf, K. & Friedl, P. Cell jamming: collective invasion of mesenchymal tumor cells imposed by tissue confinement. *Biochim. Biophys. Acta* **1840**, 2386–2395 (2014).
10. Sigismund, S. & Scita, G. The 'endocytic matrix reloaded' and its impact on the plasticity of migratory strategies. *Curr. Opin. Cell Biol.* **54**, 9–17 (2018).
11. Corallino, S., Malabarba, M. G., Zobel, M., Di Fiore, P. P. & Scita, G. Epithelial-to-mesenchymal plasticity harnesses endocytic circuitries. *Front. Oncol.* **5**, 45 (2015).
12. Palamidessi, A. et al. Endocytic trafficking of Rac is required for the spatial restriction of signaling in cell migration. *Cell* **134**, 135–147 (2008).
13. Frittoli, E. et al. A RAB5/RAB4 recycling circuitry induces a proteolytic invasive program and promotes tumor dissemination. *J. Cell Biol.* **206**, 307–328 (2014).
14. Malinverno, C. et al. Endocytic reawakening of motility in jammed epithelia. *Nat. Mater.* **16**, 587–596 (2017).
15. Giavazzi, F. et al. Giant fluctuations and structural effects in a flocking epithelium. *J. Phys. D* **50**, 384003 (2017).
16. Giavazzi, F. et al. Flocking transitions in confluent tissues. *Soft Matter* **14**, 3471–3477 (2018).
17. Mendoza, M. C. Phosphoregulation of the WAVE regulatory complex and signal integration. *Semin. Cell Dev. Biol.* **24**, 272–279 (2013).
18. Debnath, J., Muthuswamy, S. K. & Brugge, J. S. Morphogenesis and oncogenesis of MCF-10A mammary epithelial acini grown in three-dimensional basement membrane cultures. *Methods* **30**, 256–268 (2003).
19. Levitzki, A. & Gazit, A. Tyrosine kinase inhibition: an approach to drug development. *Science* **267**, 1782–1788 (1995).
20. Lang, E. et al. Coordinated collective migration and asymmetric cell division in confluent human keratinocytes without wounding. *Nat. Commun.* **9**, 3665 (2018).
21. Zeigerer, A. et al. Rab5 is necessary for the biogenesis of the endolysosomal system in vivo. *Nature* **485**, 465–470 (2012).
22. Kirchhausen, T., Owen, D. & Harrison, S. C. Molecular structure, function, and dynamics of clathrin-mediated membrane traffic. *Cold Spring Harbor Perspect. Biol.* **6**, a016725 (2014).
23. Sigismund, S. et al. Clathrin-mediated internalization is essential for sustained EGFR signaling but dispensable for degradation. *Dev. Cell* **15**, 209–219 (2008).
24. Johannes, L., Parton, R. G., Bassereau, P. & Mayor, S. Building endocytic pits without clathrin. *Nat. Rev. Mol. Cell. Biol.* **16**, 311–321 (2015).
25. Caldieri, G. et al. Reticulon 3-dependent ER-PM contact sites control EGFR nonclathrin endocytosis. *Science* **356**, 617–624 (2017).
26. Koivusalo, M. et al. Amiloride inhibits macropinocytosis by lowering submembranous pH and preventing Rac1 and Cdc42 signaling. *J. Cell Biol.* **188**, 547–563 (2010).
27. Di Guglielmo, G. M., Baass, P. C., Ou, W. J., Posner, B. I. & Bergeron, J. J. Compartmentalization of SHC, GRB2 and mSOS, and hyperphosphorylation of Raf-1 by EGF but not insulin in liver parenchyma. *EMBO J.* **13**, 4269–4277 (1994).
28. Vieira, A. V., Lamaze, C. & Schmid, S. L. Control of EGF receptor signaling by clathrin-mediated endocytosis. *Science* **274**, 2086–2089 (1996).
29. McDonald, P. H. et al. Beta-arrestin 2: a receptor-regulated MAPK scaffold for the activation of JNK3. *Science* **290**, 1574–1577 (2000).
30. Villaseñor, R., Nonaka, H., Del Conte-Zerial, P., Kalaidzidis, Y. & Zerial, M. Regulation of EGFR signal transduction by analogue-to-digital conversion in endosomes. *eLife* **4**, e06156 (2015).
31. Barrett, S. D. et al. The discovery of the benzhydroxamate MEK inhibitors CI-1040 and PD 0325901. *Bioorg. Med. Chem. Lett.* **18**, 6501–6504 (2008).
32. Kirchhausen, T., Macia, E. & Pelish, H. E. Use of dynasore, the small molecule inhibitor of dynamin, in the regulation of endocytosis. *Methods Enzymol.* **438**, 77–93 (2008).
33. Komatsu, N. et al. Development of an optimized backbone of FRET biosensors for kinases and GTPases. *Mol. Biol. Cell* **22**, 4647–4656 (2011).
34. Itoh, F. et al. The FYVE domain in Smad anchor for receptor activation (SARA) is sufficient for localization of SARA in early endosomes and regulates TGF-β/Smad signalling. *Genes Cells* **7**, 321–331 (2002).
35. Farooqui, R. & Fenteany, G. Multiple rows of cells behind an epithelial wound edge extend cryptic lamellipodia to collectively drive cell-sheet movement. *J. Cell Sci.* **118**, 51–63 (2005).
36. Alekhina, O., Burstein, E. & Billadeau, D. D. Cellular functions of WASP family proteins at a glance. *J. Cell Sci.* **130**, 2235–2241 (2017).
37. Mendoza, M. C. et al. ERK-MAPK drives lamellipodia protrusion by activating the WAVE2 regulatory complex. *Mol. Cell* **41**, 661–671 (2011).
38. Innocenti, M. et al. Abi1 is essential for the formation and activation of a WAVE2 signalling complex. *Nat. Cell Biol.* **6**, 319–327 (2004).
39. Steffen, A. et al. Sra-1 and Nap1 link Rac to actin assembly driving lamellipodia formation. *EMBO J.* **23**, 749–759 (2004).
40. Ewald, A. J., Brenot, A., Duong, M., Chan, B. S. & Werb, Z. Collective epithelial migration and cell rearrangements drive mammary branching morphogenesis. *Dev. Cell* **14**, 570–581 (2008).
41. Kim, H. Y. & Nelson, C. M. Extracellular matrix and cytoskeletal dynamics during branching morphogenesis. *Organogenesis* **8**, 56–64 (2012).
42. Carey, S. P., Martin, K. E. & Reinhart-King, C. A. Three-dimensional collagen matrix induces a mechanosensitive invasive epithelial phenotype. *Sci. Rep.* **7**, 42088 (2017).
43. Nguyen-Ngoc, K. V. et al. ECM microenvironment regulates collective migration and local dissemination in normal and malignant mammary epithelium. *Proc. Natl Acad. Sci. USA* **109**, E2595–E2604 (2012).
44. Miller, F. R., Santner, S. J., Tait, L. & Dawson, P. J. MCF10DCIS.com xenograft model of human comedo ductal carcinoma in situ. *J. Natl Cancer Inst.* **92**, 1185–1186 (2000).
45. Dvorak, H. F. Tumors: wounds that do not heal. Similarities between tumor stroma generation and wound healing. *N. Engl. J. Med.* **315**, 1650–1659 (1986).
46. Vader, D., Kabla, A., Weitz, D. & Mahadevan, L. Strain-induced alignment in collagen gels. *PLoS ONE* **4**, e5902 (2009).
47. Storm, C., Pastore, J. J., MacKintosh, F. C., Lubensky, T. C. & Janmey, P. A. Nonlinear elasticity in biological gels. *Nature* **435**, 191–194 (2005).
48. Munster, S. et al. Strain history dependence of the nonlinear stress response of fibrin and collagen networks. *Proc. Natl Acad. Sci. USA* **110**, 12197–12202 (2013).
49. Staneva, R., Barbazan, J., Simon, A., Vignjevic, D. M. & Krndija, D. Cell migration in tissues: explant culture and live imaging. *Methods Mol. Biol.* **1749**, 163–173 (2018).
50. Yang, P. S. et al. Rab5A is associated with axillary lymph node metastasis in breast cancer patients. *Cancer Sci.* **102**, 2172–2178 (2011).
51. Das, T. et al. A molecular mechanotransduction pathway regulates collective migration of epithelial cells. *Nat. Cell Biol.* **17**, 276–287 (2015).
52. Mongera, A. et al. A fluid-to-solid jamming transition underlies vertebrate body axis elongation. *Nature* **561**, 401–405 (2018).
53. Dang, T. T., Esparza, M. A., Maine, E. A., Westcott, J. M. & Pearson, G. W. ΔNp63α promotes breast cancer cell motility through the selective activation of components of the epithelial-to-mesenchymal transition program. *Cancer Res.* **75**, 3925–3935 (2015).

Acknowledgements

This work has been supported by: the Associazione Italiana per la Ricerca sul Cancro (AIRC) to G.S. (IG#18621), P.P.D.F (IG#18988 and MCO 10.000), and F.G.

(MFAG#22083); the Italian Ministry of University and Scientific Research (MIUR) to P.P.D.F. and G.S. (PRIN: PROGETTI DI RICERCA DI RILEVANTE INTERESSE NAZIONALE – Bando 2017#2017HWTP2K); the Italian Ministry of Health (RF-2013-02358446) to G.S. Regione Lombardia and CARIPLO foundation (Project 2016-0998) to R.C.; Worldwide Cancer Research (WCR#16-1245) to S.S. C.M. and F.G. are partially supported by fellowships from the University of Milan, E.B. from the FIRC-AIRC. We thank J. Christian (Max Planck Institute for Medical Research, Heidelberg, Germany) for help with fluorescent beads.

Author contributions

A.P., C.M. and E.F. designed and performed all the experiments and edited the manuscript. S.C. aided in generating cell lines and in the analysis of immunofluorescence and kinematic studies. E.B., S.S. and P.P.F.D. conceived the internalization assays and interpreted the trafficking results. G.V.B. performed EM studies. E.M., M.G. and D.P. aided in all the imaging acquisition, FRET and PIV analysis. C.T aided in the analysis of RAB5A expression in breast cancer. Q.L. and F.A. performed and analysed the AFM measurements. F.G. and R.C. analysed all the kinematic data, developed the tools for 3D motility and mechanical analysis, edited the manuscript and conceived part of the study together with C.M. E.A.C.-A helped in setting up the fluorescent bead assay. G.S. conceived the whole study, wrote the manuscript and supervised all the work. C.M., F.G., R.C. and G.S. are all equally responsible for this work.

Competing interests

The authors declare no competing interests.

Additional information

Supplementary information is available for this paper at https://doi.org/10.1038/s41563-019-0425-1.

Reprints and permissions information is available at www.nature.com/reprints.

Correspondence and requests for materials should be addressed to C.M., F.G., R.C. or G.S.

Publisher's note: Springer Nature remains neutral with regard to jurisdictional claims in published maps and institutional affiliations.

Methods

Plasmids, antibodies and reagents. Doxycycline-inducible lentiviral vectors, pSLIK-neomycin (neo) carrying RAB5A or RAB5C sequences and pSLIK-hygromycin (hygro) carrying the RAB5B sequence were obtained from Gateway Technology (Invitrogen), and prepared following the manufacturer's protocol. The plasmids pBABE-puromycin (puro)-mCHERRY-H2B and pBABE-puro-EGFP-H2B were provided by the IFOM Imaging Facility. The lentiviral expression construct pRRL-LifeAct-EGFP-puromycin (puro) was a gift from O. Pertz (University of Basel, Basel, Switzerland). The pBABE-Puro-MEK-S218D/S222D (MEK-DD) vector was purchased from Addgene.

The FRET EKAREV-ERK1/2 sensor[53] was generated by cloning the synthetized FYVE domain of SARA into the BamHI/EcoRI cleaved EKAREV-FRET vector to generate the pPBbsr2-3560NES-EKAREV-FRET vector.

Mouse monoclonal antibodies raised against α−tubulin (catalogue (cat.) no. T5168) or vinculin (cat. no. V9131) were from Sigma-Aldrich (dilution 1:400). Rabbit polyclonal anti-RAB5A (S-19, cat. no. sc-309) and goat polyclonal anti-EEA-1 (N-19, cat. no. sc-6415) antibodies were from Santa Cruz Biotechnology (dilution 1:400). Monoclonal rabbit anti-human RAB5A (cat. no. ab109534, dilution 1:100, Abcam EPR5438) was used of immunohistochemistry (IHC). Rabbit polyclonal anti-Giantin (cat. no. PRB-114C) antibody was from Covance. Mouse monoclonal anti-human Ki-67 antigen (MIB-1, cat. no. M7240) antibody was from Dako (1:1,000). Mouse monoclonal anti-AP50 (AP2mu) (31/AP50, cat. no. 611350) was from BD Bioscience. Mouse monoclonal anti-E-cadherin (cat. no. 610181) antibody was from Transduction Lab (dilution 1:1,000). Rabbit polyclonal anti-phospho-EGFR (Tyr1086, cat. no. 2220), rabbit monoclonal anti-phospho-p44/42 MAPK (ERK1/2) (Thr202/Tyr204, cat. no. 4370), rabbit polyclonal anti-p44/42 MAPK (ERK1/2) (cat. no. 9102), rabbit monoclonal anti-phospho-p38 MAPK (Thr180/Tyr182, 3D7, cat. no. 9215), mouse monoclonal anti-p38 MAPK (L53F8, cat. no. 9228), rabbit monoclonal anti-phospho-AKT (Ser473, 193H12, cat. no. 4058), rabbit polyclonal anti-AKT (cat. no. 9272), rabbit polyclonal anti-MEK1/2 (cat. no. 9122) and rabbit polyclonal anti-cleaved caspase-3 (Asp175, cat. no 9661) antibodies were from Cell Signalling Technology (dilution 1:1,000). Rabbit polyclonal anti-phospho-WAVE2 (Ser343, cat. no. 07-1512), rabbit polyclonal anti-phospho-WAVE2 (Ser351, cat. no. 07-1514) and mouse monoclonal anti-laminin-V (P3H9-2, cat. no. MAB1947) antibodies were from Merck/Millipore (dilution 1:500). Mouse monoclonal anti-WAVE2 and mouse monoclonal anti-ABI1 antibodies were homemade[54] (dilution 1:100). Rabbit polyclonal anti-NAP1 antibody was a gift from T. Stradal (Helmholtz Centre for Infection Research, Braunschweig, Germany)[55]. Rabbit polyclonal anti EGFR (806), directed against aa 1172–1186 of human EGFR (ImmunoBlot) and mouse monoclonal anti-EGFR (m108 hybridoma) directed against the extracellular domain of human EGFR (immunofluorescence) were a gift from P. P. Di Fiore (dilution 1:1,000). Secondary antibodies conjugated to horseradish peroxidase were all used at a dilution of 1:2,000 and were from: Bio-Rad (cat. nos. 7074 and 7076); Cy3-secondary antibodies from Jackson ImmunoResearch (cat. nos. 711-165-152 and 715-165-150); DAPI (cat. no. D-1306) and AlexaFluor 488 (A-11055 and A-21202) were from Thermo Fisher Scientific. TRITC (cat. no. P1951)- and FITC (cat. no. P5282)-conjugated phalloidin were from Sigma Aldrich.

Doxycycline hyclate (cat. no. D9891), dynasore hydrate (cat. no. D7693), AG1478 (cat. no. T4182), 5-(*N*-ethyl-*N*-isopropyl)amiloride (cat. no. 1154-25-2) and CK666 (cat. no. SML0006) were from Sigma Aldrich. PD0325901 (cat. no. 444966) was from Merck/Millipore. SCH772984 (cat. no. 942183-80-4) was from Selleckchem. FluoSpheres Sulfate Microspheres, 0.2 µm, yellow–green fluorescent (505/515), 2% solids (cat. no. F8848) were from ThermoFisher. Mitomycin C (cat. no. M0503) was from Sigma Aldrich.

Cell cultures and transfection. MCF10A cells were a gift from J. S. Brugge (Department of Cell Biology, Harvard Medical School, Boston, USA) and were maintained in Dulbecco's modified Eagle's medium:Nutrient Mixture F-12 (DMEM/F12) medium (Biowest) supplemented with 5% horse serum, 1% l-glutamine (EuroClone), 0.5 mg ml^{-1} hydrocortisone (Sigma-Aldrich), 100 ng ml^{-1} cholera toxin (Sigma-Aldrich), 10 µg ml^{-1} insulin (Sigma-Aldrich) and 20 ng ml^{-1} EGF (Vinci Biochem). MCF10.DCIS.com cells were provided by J. F. Marshall (Barts Cancer Institute, Queen Mary University of London, UK) and maintained in DMEM/F12 medium supplemented with 5% horse serum, 1% l-glutamine, 0.5 mg ml^{-1} hydrocortisone, 10 µg ml^{-1} insulin and 20 ng ml^{-1} EGF. All cell lines have been authenticated by cell fingerprinting and tested for mycoplasma contamination. Cells were grown at 37 °C in an humidified atmosphere with 5% CO_2. Phoenix-AMPHO cells (American Type Culture Collection, CRL-3213) were used as the packaging cell line for the generation of retroviral particles and cultured as recommended by the supplier. HEK293T cells were obtained from the BBCF-Biological Bank and Cell factory, INT, Milan and grown in DMEM supplemented with 10% fetal bovine serum and 2 mM l-glutamine and used as the packaging line for lentiviral vectors. MCF10A cells were infected with pSLIK-neo-EV (empty vector, CTR), pSLIK-neo-RAB5A, pSLIK-hygro-RAB5B or pSLIK-neo-RAB5C lentiviruses and selected with the appropriate antibiotic to obtain stable inducible cell lines. MCF10.DCIS.com were infected with pSLIK-neo-EV (empty vector, CTR) or pSLIK-neo-RAB5A lentiviruses and selected with the appropriate antibiotic to obtain stable inducible cell lines. Constitutive expression of EGFP-LifeAct, mCherry or EGFP-H2B was achieved by lentiviral and retroviral infection of MCF10A and MCF10DCIS.com cells with EGFP-LifeAct-puro or pBABE-puro-mCherry-H2B/pBABE-puro-EGFP-H2B vectors, respectively.

Transfections were performed using either calcium phosphate or FuGENE HD Transfection Reagent (cat. no. E2311, Promega), according to the manufacturer's instructions. FuGENE HD Transfection Reagent was used for FRET-EKAREV-ERK1/2 transfection in MCF10A cells.

Generation of lentiviral and retroviral particles. Packaging of lentiviruses or retroviruses was performed following standard protocols. Viral supernatants were collected and filtered through 0.45 µm filters. Cells were subjected to four cycles of infection and selected using the appropriate antibiotic: neomycin for the pSLIK-neo vector (150 µg ml^{-1}), hygromycin for the pSLIK-hygro vector (100 µg ml^{-1}) or puromycin for the EGFP-LifeAct or pBABE vectors (2 µg ml^{-1}). After several passages, stable bulk populations were selected and induced by doxycycline hyclate (2.5 µg ml^{-1}) in order to test: (1) induction efficiency by western blotting and quantitative reverse-transcription polymerase chain reaction (qRT-PCR), and (2) the homogeneity of the cell pool by immunofluorescence staining, as previously shown[14].

RNA interference. siRNA delivery was achieved by mixing 1 nM of specific siRNAs with Optimem and Lipofectamine RNAiMAX Transfection Reagent (Life Technologies). The first cycle of interference (reverse transfection) was performed on cells in suspension. The day after, a second cycle of interference (forward transfection) was performed on cells in adhesion. The following siRNAs were used for knocking down specific genes. All sequences are 5′ to 3′.

Dynamin2 (DNM2): 5′-GACATGATCCTGCAGTTCA-3′ (Dharmacon).

Clathrin heavy chain (CLTC): 5′-UAAAUUUCCGGGCAAAGAGCCCCC-3′ (Riboxx).

NCKAP1 (NAP1): 5′-CUCGAAAUCUCAUCACUGATT-3′ (Silencer Select, Ambion).

WASF4 (WAVE2): 5′-AGACCCUUCAUACUUCUUUTT-3′ (Silencer Select, Ambion).

Reticulon 3 (RTN3) (Smart pool, Dharmacon):
5′-CAAUAUGAGAAUUCAGCGA-3′
5′-GGAAAUUGUCUACGUGUCU-3′
5′-GGGAAUAUGCACUGGCGAG-3′
5′-AAGGAAAGGCUCCGCCAUU-3′

Reticulon 3 (RTN3): 5′-CCCUGAAACUCAUUAUUCGUCUCUU-3′ (Stealth, Invitrogen).

Reticulon 4 (RTN4): 5′-CCAGCCUAUUCCUGCUGCUUUCAUU-3′ (Stealth, Invitrogen).

For each RNA interference experiment, a negative control was performed with the same amount of scrambled siRNAs. Silencing efficiency was controlled by qRT-PCR.

Quantitative RT-PCR analysis. Quantitative RT-PCR analysis was performed as previously described[14]. Total RNA was extracted using the RNeasy Mini kit (Qiagen) and quantified by NanoDrop to assess both concentration and quality of the samples. Reverse transcription was performed using the SuperScript VILO cDNA Synthesis kit from Invitrogen. Gene expression was analysed by using the TaqMan Gene expression Assay (Applied Biosystems). 0.1 ng of cDNA was amplified, in triplicate, in a reaction volume of 25 µl with 10 pmol of each gene-specific primer and the SYBR Green PCR MasterMix (Applied Biosystems). Real-time PCR was performed on the 14 ABI/Prism 7700 Sequence Detector System (PerkinElmer/Applied Biosystems) using a pre-PCR step of 10 min at 95 °C, followed by 40 cycles of 15 s at 95 °C and 60 s at 60 °C. Specificity of the amplified products was confirmed by melting curve analysis (Dissociation Curve TM; Perkin Elmer/Applied Biosystems) and by 6% PAGE. Preparations with RNA template without reverse transcription were used as negative controls. Samples were amplified with primers for each gene (for details see the quantitative PCR primer list below) and GAPDH as a housekeeping gene. The cycle threshold C_t values were normalized to the GAPDH curve. PCR experiments were performed in triplicate and standard deviations calculated and displayed as error bars. Primer assay IDs were: GAPDH, Hs99999905_m1; RAB5A, Hs00702360_s1; RAB5B, Hs00161184_m1; RAB5C, Hs00428044_m1; dynamin2 (DNM2), Hs00974698_m1; clathrin heavy chain (CLTC), Hs00964480_m1; NAP1, Hs00980236_m1; WAVE2, Hs00819075_gh; reticulon3 (RTN3), Hs01581965_m1; reticulon4 (RTN4), Hs01103689_m1.

Immunoblotting. For protein extraction, cells, previously washed with cold phosphate-buffered saline (PBS), were lysed in JS buffer supplemented with proteases and phosphatases inhibitors (50 mM HEPES pH 7.5, 50 mM NaCl, 1% glycerol; 1% Triton X-100, 1.5 mM $MgCl_2$; 5 mM EGTA plus protease inhibitor cocktail (Roche Basel, Switzerland), 1 mM DTT, 20 mM Na pyrophosphate pH 7.5, 50 mM NaF, 0.5 M Na vanadate in HEPES pH 7.5 to inhibit phosphatases). Lysates were incubated on ice for 10 min and cleared by centrifugation at 13,000 r.p.m. for 30 min at 4 °C. Protein concentration was quantified by the Bradford colorimetric protein assay. The same amount of protein lysates was loaded onto polyacrylamide

gel in 5X SDS sample buffer. Proteins were transferred onto Protran Nitrocellulose Transfer membranes (Whatman), probed with the appropriate antibodies and visualized with ECL western blotting detection reagents (GE Healthcare). Membrane blocking and incubation in primary or secondary antibodies were performed for 1 h in TBS/0.1% Tween/5% milk for antibodies recognizing the total proteins or in TBS/0.1% Tween/5% bovine serum albumin (BSA) for antibodies recognizing phosphorylated proteins.

Uncropped gels of the main immunoblots are presented in Supplementary Figs. 11 and 12.

Immunohistochemistry on DCIS and IDC. Sections from archival human breast cancer samples were collected from the archives of the Tumor Immunology Laboratory of the Human Pathology Section, Department of Health Sciences, University of Palermo, Italy.

Immunohistochemistry was performed using a polymer detection method (Novolink Polymer Detection Systems Novocastra, Leica Biosystems, Newcastle, product no. RE7280-K).

Tissue samples were fixed in 10% buffered formalin and embedded in paraffin. Four-micrometre-thick tissue sections were dewaxed and rehydrated. The antigen unmasking technique was performed using Novocastra Epitope Retrieval Solution pH 6 citrate-based buffer in a thermostatic water bath at 98 °C for 30 min. Subsequently, the sections were brought to room temperature and washed in PBS–Tween. After neutralization of the endogenous peroxidases with 3% H_2O_2 and protein blocking by a specific protein block, the samples were incubated for 1 h with monoclonal rabbit anti-human RAB5A (EPR5438) (ab109534) (dilution 1:100, Abcam). Staining was revealed by a polymer detection kit (Novocastra, Ltd) and 3-amino-9-ethylcarbazole (AEC) substrate chromogen. The slides were counterstained with Harris haematoxylin (Novocastra, Ltd). All the sections were analysed under a Zeiss Axio Scope A1 optical microscope (Zeiss, Germany) and microphotographs were collected using an Axiocam 503 Color digital camera with the ZEN2 imaging software (blue edition) (Zeiss Germany).

For quantitative analysis of RAB5A IHC, non-overlapping areas, each corresponding to a ×400 high-power microscopic field, were selected from digital slide scans obtained using an Aperio CS2 slide scanner (Leica Microsystems). A total of 80 fields corresponding to DCIS fields, fields with in situ and associated infiltrating foci, and overtly infiltrative IDC fields were analysed. The percentage of strong positive cells (+3 score) per field was determined using the Aperio ImageScope software and the Positive Pixel Count v9 Algorithm (Leica Microsystems).

In situ mRNA hybridization on DCIS and IDC. In situ mRNA hybridization for the *RAB5A* transcript was performed on 4-µm-thick formalin-fixed paraffin-embedded sections of DCIS and IDC. The RNAscope 2.0 HD Reagent Kit (Advanced Cell Diagnostics, Hayward, CA, USA) was adopted according to the manufacturer's instructions, using an ad-hoc-designed *RAB5A*-specific probe (C1 Custom Probe-Hs-*RAB5A* (targeting 424-2098 of NM_001292048.1)).

All the slides were analysed under a Zeiss Axio Scope A1 optical microscope (Zeiss, Germany) and microphotographs were collected using an Axiocam 503 Color digital camera with the ZEN2 imaging software (Zeiss Germany).

Cell streaming and wound healing assays. As previously shown[14], cells were seeded in six-well plates (1.5×10^6 cells per well) in complete medium and cultured until a uniform monolayer had formed. RAB5A expression was induced, where indicated, 16 h before performing the experiment by adding fresh complete media supplemented with 2.5 µg ml^{-1} doxycycline hyclate to cells. Comparable cell confluence was tested by taking pictures by differential interference contrast imaging using a 10× objective and counting the number of nuclei per field. In the cell streaming assay, the medium was refreshed before imaging began. In the wound healing assay, the cell monolayer was scratched with a pipette tip and carefully washed with 1X PBS to remove floating cells and to create a cell-free wound area. The closure of the wound was monitored by time-lapse microscopy. An Olympus ScanR inverted microscope with 10× objective was used to take pictures every 5–10 min over a 24 h period (as indicated in the captions of Figs. 1a,b and 5a). The assay was performed using an environmental microscope incubator set to 37 °C and 5% CO_2 perfusion. After cell induction, doxycycline hyclate was maintained in the media for the total duration of the time-lapse experiment. The percentage of area covered by cells (area coverage %) over time and wound-front speed were calculated by MatLab software. In the chemical inhibitors' experiments, the inhibitor was added together with doxycycline hyclate in fresh media 1 h before starting imaging. For the cell streaming assay performed on interfered cells, cells were interfered in suspension (first cycle) and directly plated at the desired concentration, following the same conditions already described in the 'RNA interference' section.

For detection of cryptic lamellipodia, MCF10A cells stably expressing EGFP-LifeAct were mixed in a 1:10 ratio with unlabelled cells and seeded in the cell streaming assay, as described before. Cell migration was monitored by time-lapse phase contrast and fluorescence microscopy, collecting images at multiple stage positions in each time loop. An Olympus ScanR inverted microscope with a 20× objective (+1.6× Optovar) or with a Leica AM TIRF MC mic with HCX PL APO 63×/1.47 numerical aperture (NA) objective and equipped with Andor iXon DU-8285_VP was used to take pictures every 90 s. For protrusion velocity analysis, the morphodynamic quantification was performed using the ImageJ plugin ADAP (automated detection and analysis of protrusion)[56].

Each assay was done five times and at least 25 cells per condition were counted in each experiment. Where indicated, PD0325901 or SCH772984 was added 1 h before imaging.

FRET analysis. Using a customized macro in ImageJ, FRET data were analysed using the ratiometric approach. Cyan fluorescent protein (CFP), yellow fluorescent protein (YFP) and FRET images were background subtracted, converted in 32 bits and the smoothed YFP images were tresholded and used as a mask to highlight the vesicular-like structures of interest. On these areas the average FRET/CFP ratio was then calculated as described in ref. [57].

3D morphogenesis assay. The MCF10A morphogenesis assay was performed as previously described[58]. Briefly, MCF10A cells were trypsinized and resuspended in MCF10A culture medium. Eight-well chamber slides (cat. no. 80826 IBIDI) were coated with 40 µl per well of Growth Factor Reduced Matrigel Matrix Basement Membrane 10.2 mg ml^{-1} (cat. no. 354263, Corning) or with a 1:1 mixture of Matrigel HC 10.2 mg ml^{-1} and type I bovine collagen 3 mg ml^{-1} (cat. no. 5005 Advanced BioMatrix). Once the matrix was polymerized, 2.5×10^3 cells were plated into each well on top of the matrix layer in culture medium supplemented with 2% Matrigel HC 10.2 mg ml^{-1} and 5 ng ml^{-1} EGF. Complete acini morphogenesis was allowed by incubating the cells for three weeks and replacing assay media every four days.

On day 21 acini were treated with 2.5 µg ml^{-1} doxycycline hyclate to induce RAB5A expression. Cells were maintained under stimulation for six days, changing the medium every two days, before fixation with 4% paraformaldehyde and staining with specific antibodies. When inhibitors were used, the media were refreshed every day.

3D spheroid kinematic assay. MCF10DCIS.com cells were plated on ultra-low-attachment-surface six-well plates (cat. no. 3471 Corning) at a density of 5×10^3 cells per well. Cells were grown in serum-free conditions for 10 days by adding fresh culture media every 2 days. Then spheres from every single well were collected and resuspended in 150 µl of 6 mg ml^{-1} collagen type I (cat. no 35429 Corning), and diluted in culture media, 50 mM Hepes, 0.12 $NaHCO_3$ and 5 mM NaOH. The unpolymerized mix of spheres/collagen was placed in eight-well chamber slides and incubated at 37 °C overnight. The following day, before imaging, 2.5 µg ml^{-1} doxycycline hyclate was added to the polymerized collagen mix to induce RAB5A expression. For the collagen mechanical stress analysis, 20 µl of FluoSpheres Sulfate Microspheres, 0.2 µm (cat. no. F8848 ThermoFisher) were added to the unpolymerized mix of spheres/collagen and the protocol was carried out following the same conditions as previously described.

Ex vivo DCIS tumour slice motility assay. All animal experiments were approved by the OPBA (Organisms for the well-being of the animal) of IFOM and Cogentech. All experiments complied with national guidelines and legislation for animal experimentation. All mice were bred and maintained under specific pathogen-free conditions in our animal facilities at Cogentech Consortium at the FIRC Institute of Molecular Oncology Foundation and at the European Institute of Oncology in Milan, under the authorization from the Italian Ministry of Health (Autorizzazione N° 604-2016).

For mammary fat pad tumour development in NSG mice MCF10DCIS.com cells were trypsin detached, washed twice and resuspended in PBS to a final concentration 2×10^5 per 13 µl. The cell suspension was then mixed with 5 µl growth factor-reduced Matrigel and 2 µl Trypan blue solution and maintained on ice until injection. Aseptic conditions under a laminar flow hood were used throughout the surgical procedure. Female NOD.Cg-PrkdcscidIl2rgtm1Wjl/SzJ (commonly known as the NOD SCID gamma; NSG) mice, 6–9 weeks old, were anaesthetized with 375 mg kg^{-1} Avertin, laid on their backs and injected with a 20 µl cell suspension directly in the fourth mammary fad pad. After four weeks, mice were killed and the primary tumours were removed, cut by a scalpel and each tumour slide was placed over a metal grid inserted in a six-well plate to allow tumours to grow on an interface air/culture medium. Before imaging, 2.5 µg ml^{-1} doxycycline hyclate was added to the tumour slices culture media to induce RAB5A expression. Tumour cells were maintained under stimulation for three days, changing the medium every day.

Immunofluorescence. As previously described[14], cells were fixed in 4% paraformaldehyde and permeabilized with 0.1% Triton X-100 and 1% BSA for 10 min (except for EEA-1 staining, permeabilized with 0.02% Saponin and 1% BSA for 10 min, and pERK1/2 staining, permeabilized with ice cold 100% methanol for 10 min). In EGFR staining experiments, the permeabilization step was avoided where indicated (non-permeabilized conditions) in order to detect only total cell surface EGFR. After a 1X PBS wash, primary antibodies were added for 1 h at room temperature. Coverslips were washed in 1X PBS before secondary antibody incubation for 1 h at room temperature, protected from light. FITC- or TRITC-

phalloidin was added in the secondary antibody step, where applicable. After removal of not specifically bound antibodies by 1X PBS washing, nuclei were stained with 0.5 ng ml^{-1} DAPI. Samples were post-fixed and mounted on glass slides in anti-fade mounting medium (Mowiol). Antibodies were diluted in 1X PBS and 1% BSA. Images were acquired by a wide-field fluorescence microscope or confocal microscope, as indicated in the figure legends.

Immunofluorescence on MCF10A-derived acini was performed by fixing acini with 4% paraformaldehyde for 20 min at room temperature. Then, cells were permeabilized with 0.5% Triton X-100 in PBS for 10 min at 4 °C and incubated with blocking solution (PBS/0.1% BSA/10% goat serum) for 1 h at room temperature. Acini were incubated with indicated primary antibodies diluted in blocking solution overnight at 4 °C. The following day, acini were incubated with indicated secondary antibodies diluted in blocking solution for 1 h at room temperature. Finally, acini were incubated with DAPI in PBS for 20 min at room temperature. Samples were then maintained at 4 °C in PBS before imaging.

E-cadherin staining was analysed by confocal microscopy and images were processed to obtain the straightness index of the junction. 'Junction length' was measured by tracking a straight line and 'junction tracking' was obtained by tracking manually the same junction following its profile. The straightness index of the junction is quantified as the ratio of the junction length and the junction tracking.

^{125}I-EGF internalization assay. Internalization of ^{125}I-EGF was performed at low (1 ng ml^{-1}) or high (30 ng ml^{-1}) EGF concentrations as described in ref. [25].

Briefly, MCF10A cells were plated in 24-well plates in at least duplicate for each time point, plus one well to assess non-specific binding. Cell monolayers were EGF-starved for 24 h and induced overnight by doxycycline hyclate. The following day, cells were incubated in assay medium (DMEM/F12 supplemented with cholera toxin (100 ng ml^{-1}), 0.1% BSA, 20 mM HEPES, doxycycline hyclate (2.5 µg ml^{-1})) and then incubated at 37 °C in the presence of 1 ng ml^{-1} ^{125}I-EGF or 30 ng ml^{-1} EGF (1 ng ml^{-1} ^{125}I-EGF (Perkin Elmer) + 29 ng ml^{-1} cold EGF). At different time points (2, 4, 6 min), the amount of bound ^{125}I-EGF was measured with an acid wash solution pH 2.5 (0.2 M acetic acid, 0.5 M NaCl). Cells were then lysed with 1 N NaOH, which represents the amount of internalized ^{125}I-EGF. Non-specific binding was measured at each time point in the presence of an excess of non-radioactive EGF (300 times). After being corrected for non-specific binding, the rate of internalization was calculated as the ratio between internalized and surface-bound radioactivity. Surface EGFRs were measured by ^{125}I-EGF saturation binding as described[23].

EGF recycling assay. Recycling assays of ^{125}I-EGF were performed as described in ref. [23]. In brief, cell monolayers were EGF-starved for 24 h and induced overnight by doxycycline hyclate. The following day, cells were incubated in assay medium (DMEM/F12 supplemented with cholera toxin (100 ng ml^{-1}), 0.1% BSA, 20 mM HEPES, doxycycline hyclate (2.5 µg ml^{-1})), then incubated with ^{125}I-EGF (30 ng ml^{-1}: 5 ng ml^{-1} of ^{125}I-EGF + 25 ng ml^{-1} of cold EGF) for 15 min at 37 °C, followed by a mild acid/salt treatment (buffer at pH 4.5, 0.2 M Na acetate pH 4.5, 0.5 M NaCl) to remove bound EGF. Cells were then chased at 37 °C in a medium containing 4 µg ml^{-1} EGF for the indicated times, to allow internalization and recycling. At the end of each chase time, the medium was collected, half was counted directly (free) and half was subjected to trichloroacetic acid (TCA) precipitation to determine the amount of intact/recycled (TCA-precipitable) and degraded (TCA-soluble) ^{125}I-EGF present in it. Surface-bound ^{125}I-EGF was extracted by an acid treatment (0.5 M NaCl, 0.2 M acid acetic). Finally, cells were lysed in 1 N NaOH to determine intracellular ^{125}I-EGF. Data are expressed as the fraction of intact ^{125}I-EGF in the medium with respect to the total (total medium + total surface + total intracellular). Non-specific counts were measured for each time point in the presence of a 300-fold excess of cold ligand, and were never >3–10 % of the total counts.

Image acquisition. Time-lapse imaging of the motility of 3D acini/spheroids was performed on a Leica TCS SP8 laser confocal scanner mounted on a Leica DMi8 microscope equipped with motorized stage; a HC PL FLUOTAR 20×/0.5 NA dry objective was used. A white-light laser was used as the illumination source. Leica Application Suite X (LAS X, https://www.leica-microsystems.com/products/microscope-software/details/product/leica-las-x-ls/) was the software used for all the acquisitions.

Image acquisition conditions were set to remove channel crosstalk, optimizing spectral detection bands and scanning modalities. ImageJ software was used for data analysis.

Collagen second-harmonic generation analysis on collagen-embedded MCF10DCIS spheroids was performed with a confocal microscope (Leica; TCS SP5) on an upright microscope (DM6000 CFS) equipped with blue (argon, 488 nm), yellow (561 nm solid-state laser) and red (633 nm solid-state laser) excitation laser lines with an HCX PL APO 40×/1.25–0.75 NA oil-immersion objective and controlled by Leica LAS AF Lite software (Leica). We used a two-photon excitation technique with a pulsed infrared laser (Chameleon Ultra II; Coherent) at 980 nm.

EKAREV FRET analysis was performed using a DeltaVision Elite imaging system (Applied Precision) controlled by softWoRx Explorer 2.0 (Applied Precision) equipped with a DV Elite CMOS camera and an inverted microscope (IX71; Olympus) using a PlanApo N 60×/1.42 NA oil-immersion objective lens.

The ex vivo DCIS tumour slice motility assay was performed using an Olympus IX83 inverted microscope controlled by The Olympus cellSens Standard software (Olympus, https://www.olympus-lifescience.com/en/software/cellsens/) and equipped with an iXon Ultra Andor (EMCCD) 16 bit camera using an UplanSApo 10×/0.4 NA dry objective.

Atomic force microscopy (AFM) measurements of collagen gels. Collagen gel samples at different concentrations (2, 4, 6 mg ml^{-1}) were prepared as previously described in wells obtained by binding a microfabricated polydimethylsiloxane ring (height = 2 mm, outer diameter = 10 mm, inner diameter = 6 mm) to 24-mm-round glass coverslips via plasma treatment of the surfaces.

The stiffness of collagen gel samples was measured at 37 °C by using NanoWizard3 AFM (JPK, Germany) coupled to an Olympus inverted microscope. A silicon nitride AFM probe (nominal spring constant of 0.03 N m^{-1}: NovaScan, USA) functionalized with a borosilicate microsphere (10 µm in diameter) was used for AFM indentation. Before the measurements, the deflection sensitivity and spring constant of the cantilever were calibrated in PBS on glass at 37 °C.

Collagen gel stiffness was measured by bringing the bead-functionalized cantilever tip into contact with the matrix surface at 30 (or more) different positions. For each position five force curves were recorded. The contact force was set at a threshold value of 2 nN, the approach–retraction distance was 10 µm, and the approach velocity was 10 µm s^{-1}.

The data points below 0.8 µm indentation depth were used to calculate the elastic (Young) modulus, by fitting the curves with the Hertz model:

$$F = \frac{4}{3}\frac{E}{(1-\nu^2)}\sqrt{R\delta^3} \quad (1)$$

where F is the indentation force, E is the Young modulus to be determined, ν is the Poisson ratio, R is the radius of the spherical bead and δ is the indentation depth.

Electron microscopy. Electron microscopic examination was performed as previously described[59,60]. A description of each process is described below.

Embedding: the tissue and 3D spheroids were fixed with a 4% paraformaldehyde and 2.5% glutaraldehyde (EMS, USA) mixture in 0.2 M sodium cacodylate pH 7.2 for 2 h at room temperature, followed by six washes in 0.2 sodium cacodylate pH 7.2 at room temperature. Then, cells were incubated in a 1:1 mixture of 2% osmium tetraoxide and 3% potassium ferrocyanide for 1 h at room temperature followed by six times rinsing in 0.2 M cacodylate buffer. Then, the samples were sequentially treated with 0.3% thiocarbohydrazide in 0.2 M cacodylate buffer for 10 min and 1% osmium tetraoxide in 0.2 M cacodylate buffer (pH 6.9) for 30 min. Then, samples were rinsed with a 0.1 M sodium cacodylate (pH 6.9) buffer until all traces of the yellow osmium fixative had been removed, washed in deionized water, treated with 1% uranyl acetate in water for 1 h and washed in water again[59,60]. The samples were subsequently subjected to dehydration in ethanol and then in acetone and embedded in epoxy resin at room temperature and polymerized for at least 72 h in a 60 °C oven. Embedded samples were then sectioned with a diamond knife (Diatome, Switzerland) using a Leica ultramicrotome (Leica EM UC7; Leica Microsystems, Vienna). Sections were analysed with a Tecnai 20 High Voltage Electron Microscope (FEI, Thermo Fisher Scientific, Eindhoven, the Netherlands) operating at 200 kV (ref. [60]).

Measurement of the cellular velocities and trajectories on monolayers. Coarse-grained maps of the instantaneous cellular velocities were obtained by analysing time-lapse phase-contrast movies with a custom PIV software written in MATLAB[14]. The time interval between consecutive frames was 5 min or 10 min. The interrogation window was 32 × 32 pixels (pixel size 1.29 µm or 1.6 µm), with an overlap of 50% between adjacent windows. The number of cells comprised within one field-of-view (FOV) was typically 2,500. For a given monolayer, time-lapse images from different (typically from 5 to 10) FOVs were simultaneously collected.

The instantaneous $v_{RMS}(t)$ of a cell monolayer was computed as $V_{RMS}(t) = \sqrt{\langle |\mathbf{v}(t)|^2 \rangle_{\mathbf{x},j}}$, where $\mathbf{v}(t)$ is the instantaneous velocity vector and $\langle \cdot \rangle_{\mathbf{x},j}$ indicates an average over all grid points $\mathbf{x}$ (corresponding to the centres of the PIV interrogation windows) and FOVs j, respectively.

The instantaneous order parameter $\psi(t)$ of a cell monolayer was computed as $\psi(t) = \left\langle \frac{|\langle \mathbf{v}(t) \rangle_{\mathbf{x}}|^2}{\langle |\mathbf{v}(t)|^2 \rangle_{\mathbf{x}}} \right\rangle_j$. This definition is such that $0 \leq \psi(t) \leq 1$. In particular, $\psi(t) = 1$ only if, within each FOV, the velocity field is perfectly uniform, that is, all the cells in the monolayer move with the same speed and in the same direction. On the contrary $\psi(t) \cong 0$ is expected for a randomly oriented velocity field.

The vectorial velocity correlation functions were calculated as $C_{VV}(r) = \left\langle \frac{|\langle \mathbf{v}(\mathbf{x}+\mathbf{r},t) \cdot \mathbf{v}(\mathbf{x},t) \rangle_{\mathbf{x},t}|^2}{\langle |\mathbf{v}|^2 \rangle_{\mathbf{x},t}} \right\rangle_j$. Unless otherwise stated in the main text, the

temporal average $\langle\cdot\rangle_t$ was always performed over the time window comprised between 4 and 12 h from the beginning of the image acquisition.

The velocity correlation function L_{corr} is obtained by fitting $C_{VV}(r)$ with a stretched exponential function of the form $f(r) = (1-\alpha)e^{-(r/L_{corr})^{\gamma}} + \alpha$. Here γ is a stretching exponent and α is an offset that is non-zero in presence of a collective migration of the monolayer.

Cellular trajectories $\mathbf{r}_m(t)$ were calculated by numerical integration of the instantaneous velocity field as obtained from the PIV analysis (see ref. [61] and references therein). For each FOV a number of trajectories roughly corresponding to the number of cells was computed.

Mean squared displacements (MSDs) of the cells were calculated as $\mathrm{MSD}(\Delta t) = |\mathbf{r}_m(t+\Delta t) - \mathbf{r}_m(t)|^2$, where the average was performed over all the trajectories and, unless otherwise stated in the main text, in the time window comprised between 4 and 12 h after the beginning of the experiment. To estimate the persistence length L_{pers} of the cellular motion the MSD curves were fitted with a function of the form $g(\Delta t) = (u_0\Delta t)^2[1 + (u_0\Delta t/L_{pers})]^{-1}$. This expression describes a transition between a short-time ballistic-like scaling, with characteristic speed u_0, and a long-time diffusive scaling. The transition between the two regimes takes place for $\Delta t \approx 1/u_0 L_{pers}$, that is, after the cell has travelled with an approximately constant velocity over a distance $\approx L_{pers}$.

Measurement of the cellular velocities of acini. Sequences of confocal Z stacks of 3D acini were analysed with an adapted PIV scheme to extract a representative value for the migration velocity, to assess the collective nature of the cellular motion and to detect the presence of a coherent rotational motion. Details about the imaging are given in the section 'Image acquisition'.

The geometrical centre $\mathbf{x}_c$ of each acinus was determined as the centroid of the corresponding 3D fluorescent intensity distribution (Z stack) $I(\mathbf{x},t)$: $\mathbf{x}_c = \frac{\sum I(\mathbf{x},t)\mathbf{x}}{\sum I(\mathbf{x},t)}$, where the sums are performed over all voxels and time points. For each time point, the 3D fluorescent intensity distribution was radially projected onto the unit sphere centred in $\mathbf{x}_c$ leading to a sequence of 2D intensity maps $i(\theta,\varphi|t)$, where θ and φ are the polar and the azimuthal angle spanning the sphere, respectively. In practice, $i(\theta,\varphi|t)$ was obtained from a representation of $I(\mathbf{x}|t)$ in spherical coordinates, after summation over the radial coordinate. For each time point, i is represented by a 512×128 matrix, each element covering the Cartesian product of angular intervals of constant amplitudes $\Delta\theta = \pi/512$ and $\Delta\varphi = 2\pi/128$, respectively.

We performed on i a 2D PIV analysis as described in the previous paragraph, by treating (θ,φ) as Cartesian coordinates. The obtained coarse-grained velocity fields $[u_\theta(\theta,\varphi|t), u_\varphi(\theta,\varphi|t)]$ (in units of rad h^{-1}) were then used to reconstruct the tangential velocity field $\mathbf{v}(\theta,\varphi) = R_0(u_\theta(\theta,\varphi|t)\mathbf{n}_\theta + u_\varphi(\theta,\varphi|t)\sin\theta\mathbf{n}_\varphi)$ of the acinus. Here, $\mathbf{n}_\theta$ and $\mathbf{n}_\varphi$ are the polar and the azimuthal unit vector, respectively, and $R_0 = \sqrt{\frac{\sum I(\mathbf{x},t)(\mathbf{x}-\mathbf{x}_c)^2}{\sum I(\mathbf{x},t)}}$ is the radius of gyration of the acinus.

The RMS velocity was calculated as $V_{RMS}(t) = \sqrt{\langle|\mathbf{v}|^2\rangle}$, where the angular brackets indicate an average performed over the whole sphere. The presence of a pattern of global rotation was monitored by measuring the total angular momentum $\mathbf{l} = \langle\mathbf{r}\times\mathbf{v}\rangle$, where $\mathbf{r}$ is a unit vector spanning the whole sphere. The direction of $\mathbf{l}$ identifies the orientation of the axis of instantaneous rotation. The collective nature of the cellular motility is captured by the non-dimensional rotational order parameter $\psi = \frac{\pi}{2}\frac{|\mathbf{l}|^2}{V_{RMS}^2}$. The normalization of the order parameter is such that, for a rigidly rotating sphere, $\psi = 1$, while in the absence of coordinated motion one expects $\psi \cong 0$.

Phase-contrast rotation analysis of acini. Maps of the instantaneous cellular velocities were obtained by analysing time-lapse movies and performing a PIV analysis using the MATLAB MPIV toolbox (http://www.oceanwave.jp/softwares/mpiv/ and https://www.mathworks.com/help/matlab/ref/curl.html) with the minimum quadric differences (MQD) algorithm and an interrogation window of 24 pixels × 24 pixels with an overlap of 50%. From the maps of the instantaneous cellular velocities for each frame, we computed the map of curl of the velocity field using the MATLAB function curl. For each frame, we evaluated the rotation of the acini as the average of absolute value of the curl map.

Kinematic and dynamical analysis of spheroids. Overall motility and internal dynamics of control and RAB5A-MCF10A-expressing mCherry-H2B spheroids were measured by analysing time sequences of confocal Z stacks according to the following procedure, implemented in a custom MATLAB code. More details about the imaging can be found in the section 'Image acquisition'.

We indicate with $R(\boldsymbol{\Theta},\mathbf{U})$ the roto-translational operator given by the composition of a 3D rotation by an angle $|\boldsymbol{\Theta}|$ around the axis identified by the direction of the 3D vector $\boldsymbol{\Theta}$ and a translation of vector $\mathbf{U}$. $R(\boldsymbol{\Theta},\mathbf{U})$ is a linear operator and its numerical implementation as a transformation between 3D matrices (Z stacks) was realized via the MATLAB functions imwrap and affine3d.

Let us consider two 3D stacks $I(\mathbf{x},t)$ and $I(\mathbf{x},t+\Delta t_0)$, where Δt_0 is the delay between consecutive stacks. We define $\boldsymbol{\Omega}(t)$ and $\mathbf{U}(t)$ as the 3D vectors that minimize the distance d (namely, the variance of the difference) between $I(\mathbf{x},t+\Delta t_0)$ and $R(\boldsymbol{\Omega}(t)\Delta t_0,\mathbf{U})\ I(\mathbf{x},t)$: $d(\boldsymbol{\omega},\mathbf{u}|t) = ||\ I(\mathbf{x},t+\Delta t_0) - R(\boldsymbol{\Omega}\Delta t_0,\mathbf{U})\ I(\mathbf{x},t)\ ||^2$. Numerically, the minimization is performed by exploiting the MATLAB function imregtform. In substance, $R(\boldsymbol{\Omega}(t)\Delta t_0, \mathbf{U}(t))$ is the rigid transformation that reproduces at best the changes occurred in $I(\mathbf{x},t)$ during the time interval Δt_0. According to the definitions above, $\boldsymbol{\Omega}(t)$ provides the best estimate for the instantaneous vectorial angular velocity of the spheroid, the direction of $\mathbf{n}(t) = \frac{\boldsymbol{\Omega}(t)}{|\boldsymbol{\Omega}(t)|}$ identifying the axis of instantaneous rotation. The temporal persistence of the rotational motion is captured by the orientational correlation function $C_{\mathbf{n}}(\Delta t) = \mathbf{n}(t+\Delta t)\cdot\mathbf{n}(t)_t$, where $\Delta t = n\Delta t_0$. To estimate the rotational correlation time τ_p, $C_{\mathbf{n}}(\Delta t)$ was fitted with an exponential function of the form $f(\Delta t) = \exp(-\Delta t/\tau_p)$. The residual internal restructuring dynamics is measured via a generalization to the 3D case of a recently introduced method (difference variance analysis (DVA)) for the quantification of the dynamics of particulate soft matter systems[62]. The non-rigid part of the changes occurring within a spheroid between time t and $t+\Delta t$, where $\Delta t = n\Delta t_0$, is captured by the parameter: $q(\Delta t,t) = 1-\beta^{-1}||\ I(\mathbf{x},t+\Delta t) - T(\Delta t,t)\ I(\mathbf{x},t)||^2$, where $T(\Delta t,t) = R(\boldsymbol{\Omega}(t+n\Delta t_0)\Delta t, \mathbf{U}(t+n\Delta t_0))\circ R(\boldsymbol{\Omega}(t+(n-1)\Delta t_0)\Delta t, \mathbf{U}(t+(n-1)\Delta t_0))\circ\ldots\circ R(\boldsymbol{\Omega}(t)\Delta t, \mathbf{U}(t))$ is the composition of elementary roto-translations and $\beta = 2(\langle I^2\rangle_{t,\mathbf{x}} - \langle I\rangle^2_{t,\mathbf{x}})$. The definition of q is such that, neglecting noise and truncation errors, $q \cong 1$ if the spheroid is immobile or if it undergoes a perfectly rigid displacement and/or rotation, with no relative motion between different cells. On the contrary, one gets $q \cong 0$ when almost all the cells have performed positional rearrangements on a length scale comparable with their size, leading to a substantial change in the local structure[62]. We consider the so-called overlap parameter Q, obtained as a temporal average of q: $Q(\Delta t) = \langle q(\Delta t,t)\rangle_t$.

By fitting the decay of Q with an exponential function $(\Delta t) = Q_0 e^{-\Delta t/\tau}$, we can extract an estimate of the characteristic correlation time τ after which an almost complete change in the cellular configuration has occurred.

Moreover, to spot potential spatial inhomogeneities in the dynamics, in particular a dependence of the relaxation time on the radial coordinate $r = |\mathbf{x}|$ (in a reference frame where $\mathbf{x} = 0$ corresponds to the centre of the spheroid), we also considered a space-resolved version $Q_s(\Delta t,r) = \langle q_s(\Delta t,t,\mathbf{x})\rangle_{t,|\mathbf{x}|=r}$ of the above-defined overlap parameter, where $q_s(\Delta t,t,\mathbf{x}) = 1-\beta_s^{-1}[I(\mathbf{x},t+\Delta t) - T(\Delta t,t)I(\mathbf{x},t)]^2$ and $\beta_s = 2(\langle I^2\rangle_{t,|\mathbf{x}|=r} - \langle I\rangle^2_{t,|\mathbf{x}|=r})$. According to the above definitions, the decay of $Q_s(\Delta t,r)$ captures the relaxation dynamics at different distances r from the centre of the spheroid. Instead of performing a fit, we extracted the relaxation rate $\Gamma(r) = 1/\tau(r)$ associated with the decay of $Q_s(\Delta t,r)$ as a function the delay time Δt in a simple and robust manner by considering the difference quotient at the origin of the temporal axis: $\Gamma(r) \cong -[Q_s(\Delta t_0,r) - Q_s(0,r)]/\Delta t_0$.

Reference-free estimation of the fluctuating RMS stresses using stress fluctuation microscopy. Spatial maps of the RMS stresses in the ECM surrounding MCF10.DCIS.com spheroids were obtained by analysing the positional fluctuations of embedded, fluorescent tracer particles by using stress fluctuation microscopy, as described below. The procedure was applied to 4D stacks ($xyzt$) obtained from time-lapse confocal acquisitions. Each stack included 72 time points and 35 Z planes, each plane having a resolution of 512×512 pixels. Delay between frames was 20 min, voxel size was (xyz) $0.57\times0.57\times3.00\,\mu m^3$.

The instantaneous velocity field $\mathbf{v}(\mathbf{x},t) = \partial_t\mathbf{u}(\mathbf{x},t)$ associated with the motion of the fluorescent tracers embedded in the ECM was obtained via a custom Lucas–Kanade optical flow algorithm[63] implemented in MATLAB (Gaussian weighted window ($\sigma = 2$ pixels), mesh size: 10 pixels) (Supplementary Fig. 10a,b and Supplementary Video 27). Here, $\mathbf{u}(\mathbf{x},t)$ represents the displacement field of the ECM with respect to its (unknown) mechanical equilibrium condition. We note that the time derivative of the strain tensor $\varepsilon_{ij}(\mathbf{x},t) \equiv \partial_i u_j(\mathbf{x},t)$ can be written in terms of a spatial derivative of the velocity as $\partial_t\varepsilon_{ij}(\mathbf{x},t) = \partial_i v_j(\mathbf{x},t)$. This last equality enables estimating the mean squared value (MSV) of the strain fluctuation $\Delta\varepsilon_{ij}(\tau) \equiv \varepsilon_{ij}(t_0+\tau) - \varepsilon_{ij}(t_0)$ as an integral of the temporal correlation function $C_{ij}(t) \equiv \langle\partial_i v_j(t+t_0)\partial_i v_j(t_0)\rangle$[64]

$$\langle\Delta\varepsilon_{ij}(\tau)^2\rangle = 2\int_0^\tau(\tau-|t|)C_{ij}(t)\mathrm{d}t \qquad (2)$$

where the dependence on the spatial coordinate $\mathbf{x}$ has been omitted for clarity. Temporal correlation functions $C_{ij}(t)$ evaluated in proximity of the boundary of different spheroids are shown in Supplementary Fig. 10c. We found that $\langle\Delta\varepsilon_{ij}(\tau)^2\rangle$ rapidly saturates to a τ-independent asymptotic value $\langle\Delta\varepsilon_{ij}^2\rangle$. Once the MSV $\langle\Delta\varepsilon_{ij}^2\rangle$ of the strain fluctuation is obtained, the MSV $\langle\Delta\sigma_{ij}^2\rangle$ of the stress fluctuation can be obtained via the constitutive equations of the material, which we assumed to be isotropic and homogeneous. This assumption relies on the fact that the length scales probed in our experiments (a few micrometres) are about one order of magnitude larger than the characteristic mesh size of the collagen network[58]. Moreover, we adopt the approximation of negligible compressibility (that is, that the Poisson ratio of the material is 0.5)[65]. Under these hypotheses, the mechanical response of the material is described in terms of a single parameter, namely the Young modulus E, that we measured directly with AFM indentation experiments.

In this work, the above-described procedure has been applied on the equatorial plane of each spheroid, by considering the 2D intensity distribution obtained as a z-average of three adjacent confocal planes. Therefore, only the in-plane components of the velocity, strain and stress were considered. In this simplified geometry, the diagonal components of the fluctuating stress tensor are given by

$$\langle \Delta\sigma_{11}^2 \rangle = \left(\frac{E}{1-\nu^2}\right)^2 (\langle \Delta\varepsilon_{11}^2 + \nu^2 \Delta\varepsilon_{22}^2 \rangle) \quad (3)$$

$$\langle \Delta\sigma_{22}^2 \rangle = \left(\frac{E}{1-\nu^2}\right)^2 (\langle \Delta\varepsilon_{22}^2 + \nu^2 \Delta\varepsilon_{11}^2 \rangle) \quad (4)$$

while the mean value of the normal stress can be calculated as

$$\langle \Delta\sigma^2 \rangle = E^2 \frac{(1+\nu^2)}{(1-\nu^2)^2} \langle \Delta\varepsilon^2 \rangle \quad (5)$$

where $\langle \Delta\varepsilon^2 \rangle = (\langle \Delta\varepsilon_{11}^2 + \Delta\varepsilon_{22}^2 \rangle)/2$. The level of uncertainty associated with this analysis was estimated by applying the described procedure to $n = 5$ confocal stacks collected with the same acquisition parameters in portions of the fluorescent particle-seeded collagen gel far from the embedded spheroids. The obtained MSV of the 'background' normal stress was $\langle \Delta\sigma^2 \rangle|_{bgd} = 50 \pm 3\ \mathrm{Pa}^2$, about one order of magnitude smaller than the peak values obtained in the presence of a spheroid (Supplementary Fig. 10d). We estimated the RMS value σ_{RMS} of the fluctuating stress in the presence of the spheroids by subtracting this spurious contribution from the measured MSV: $\sigma_{RMS} = \sqrt{\langle \Delta\sigma^2 \rangle - \langle \Delta\sigma^2 \rangle|_{bgd}}$. We note that, in principle, the above-described formalism could be easily adapted to reconstruct the full 3D distribution of the fluctuating stresses. Nevertheless, the limited axial resolution of the confocal acquisition system imposes a substantial limitation on the accuracy of the reconstructed tracer's displacements along z, with an obvious impact on the reconstructed stresses. The solution to this problem is beyond the scope of this work and will be investigated in future publication.

Statistical analysis. Student's unpaired and paired t-tests were used for determining the statistical significance whenever we compared in a pairwise fashion two distinct distributions. In the case of the endosome size distribution comparing multiple treatments (control, RAB5A, RAB5B and RAB5C), chi-sqaure or Mann-Whitney or Tukey tests were applied as indicated. In Supplementary Fig. 8C, P values of the Kaplan–Meier curves were calculated using a log-rank test. Significance was defined as $^{*}p < 0.05$; $^{**}p < 0.01$; $^{***}p < 0.001$ and $^{****}p < 0.0001$. Statistical calculations were performed with GraphPad Prism 8 Software (https://www.graphpad.com/scientific-software/prism/). Data are expressed as mean ± standard deviation (s.d.) unless otherwise indicated.

Reporting Summary. Further information on research design is available in the Nature Research Reporting Summary linked to this article.

Data availability

The authors declare that all data supporting the findings of this study are available within the paper and its supplementary Information files and from the corresponding authors upon reasonable request.

Code availability

The codes used for the analysis are all indicated in the Methods.

References

54. Innocenti, M. et al. Abi1 regulates the activity of N-WASP and WAVE in distinct actin-based processes. *Nat. Cell Biol.* **7**, 969–976 (2005).
55. Stradal, T. E. et al. Regulation of actin dynamics by WASP and WAVE family proteins. *Trends Cell Biol.* **14**, 303–311 (2004).
56. Barry, D. J., Durkin, C. H., Abella, J. V. & Way, M. Open source software for quantification of cell migration, protrusions, and fluorescence intensities. *J. Cell Biol.* **209**, 163–180 (2015).
57. Kardash, E., Bandemer, J. & Raz, E. Imaging protein activity in live embryos using fluorescence resonance energy transfer biosensors. *Nat. Protoc.* **6**, 1835–1846 (2011).
58. Yang, Y. L., Leone, L. M. & Kaufman, L. J. Elastic moduli of collagen gels can be predicted from two-dimensional confocal microscopy. *Biophys. J.* **97**, 2051–2060 (2009).
59. Beznoussenko, G. V., Ragnini-Wilson, A., Wilson, C. & Mironov, A. A. Three-dimensional and immune electron microscopic analysis of the secretory pathway in *Saccharomyces cerevisiae*. *Histochem. Cell Biol.* **146**, 515–527 (2016).
60. Beznoussenko, G. V. & Mironov, A. A. Correlative video-light-electron microscopy of mobile organelles. *Methods Mol. Biol.* **1270**, 321–346 (2015).
61. Park, J. A. et al. Unjamming and cell shape in the asthmatic airway epithelium. *Nat. Mater.* **14**, 1040–1048 (2015).
62. Pastore, R., Pesce, G. & Caggioni, M. Differential variance analysis: a direct method to quantify and visualize dynamic heterogeneities. *Sci. Rep.* **7**, 43496 (2017).
63. Barron, J. L., Fleet, D. J. & Beauchemin, S. S. Performance of optical flow techniques. *Int. J. Comput. Vis.* **12**, 43–77 (1994).
64. Kubo, R. The fluctuation-dissipation theorem. *Rep. Prog. Phys.* **29**, 255–284 (1966).
65. Castro, A. P. et al. Combined numerical and experimental biomechanical characterization of soft collagen hydrogel substrate. *J. Mater. Sci. Mater. Med.* **27**, 79 (2016).

nature research

Corresponding author(s): Giorgio Scita

Last updated by author(s): 03/06/2019

Reporting Summary

Nature Research wishes to improve the reproducibility of the work that we publish. This form provides structure for consistency and transparency in reporting. For further information on Nature Research policies, see Authors & Referees and the Editorial Policy Checklist.

Statistics

For all statistical analyses, confirm that the following items are present in the figure legend, table legend, main text, or Methods section.

n/a	Confirmed	
☐	☒	The exact sample size (*n*) for each experimental group/condition, given as a discrete number and unit of measurement
☐	☒	A statement on whether measurements were taken from distinct samples or whether the same sample was measured repeatedly
☐	☒	The statistical test(s) used AND whether they are one- or two-sided *Only common tests should be described solely by name; describe more complex techniques in the Methods section.*
☒	☐	A description of all covariates tested
☒	☐	A description of any assumptions or corrections, such as tests of normality and adjustment for multiple comparisons
☐	☒	A full description of the statistical parameters including central tendency (e.g. means) or other basic estimates (e.g. regression coefficient) AND variation (e.g. standard deviation) or associated estimates of uncertainty (e.g. confidence intervals)
☐	☒	For null hypothesis testing, the test statistic (e.g. *F*, *t*, *r*) with confidence intervals, effect sizes, degrees of freedom and *P* value noted *Give P values as exact values whenever suitable.*
☒	☐	For Bayesian analysis, information on the choice of priors and Markov chain Monte Carlo settings
☒	☐	For hierarchical and complex designs, identification of the appropriate level for tests and full reporting of outcomes
☒	☐	Estimates of effect sizes (e.g. Cohen's *d*, Pearson's *r*), indicating how they were calculated

Our web collection on statistics for biologists contains articles on many of the points above.

Software and code

Policy information about availability of computer code

Data collection

Data were collected using with the following software and systems:
1. For IHC: Aperio CS2 slide scanner (Leica Microsystems)
2. For FRET experiments: a customised macro in ImageJ was used and FRET data were analysed using the ratiometric approach.
3. For image acquisition: Image acquisition conditions were set to remove channel crosstalk, optimizing spectral detection bands and scanning modalities. ImageJ software was used for data analysis.
4. Coarse-grained maps of the instantaneous cellular velocities were obtained by analysing time-lapse phase-contrast movies with a custom PIV software written in MATLAB
5. Custom MatLab code used for wound healing analysis, particle image velocimetry (PIV), cellular trajectory calculations, optical flow velocimetry, 3D image registration, 3D difference variance analysis and fluctuating stress microscopy is available from the corresponding author on request.
7. for SHG we used a two-photon excitation (2PE) technique with a pulsed infrared laser (Chameleon Ultra II; Coherent) at 980 nm
8. All the sections were analyzed under a Zeiss Axio Scope A1 optical microscope (Zeiss, Germany) and microphotographs were collected using an Axiocam 503 Color digital camera with the ZEN2 imaging software (blue edition) (Zeiss Germany)
9. Time-lapse imaging of 3D acini/spheroids motility was performed on a Leica TCS SP8 laser confocal scanner mounted on a Leica DMi8 microscope equipped with motorized stage; a HC PL FLUOTAR 20X/0.5NA dry objective was used. A white light laser was used as illumination source. Leica Application Suite X (LAS X, https://www.leica-microsystems.com/products/microscope-software/details/product/leica-las-x-ls/) was the software used for all the acquisitions.
10. Collagen SHG analysis on collagen embedded MCF10DCIS spheroids was performed with a confocal microscope (Leica; TCS SP5) on an upright microscope (DM6000 CFS) equipped with blue (argon, 488 nm), yellow (561 nm solid state laser), and red (633 nm solid state laser) excitation laser lines with an HCX PL APO 40X/1.25-0.75NA oil immersion objective and controlled by Leica LAS AF Lite software (Leica).
11. Ex vivo DCIS tumor slice motility assay was performed using an Olympus IX83 inverted microscope controlled by The Olympus cellSens Standard software (Olympus, https://www.olympus-lifescience.com/en/software/cellsens/) and equipped with an iXon Ultra Andor (EMCCD) 16 bit camera using a UplanSApo 10X/0.4NA dry objective.

Data analysis	1. for IHC: Aperio ImageScope software and the Positive Pixel Count v9 Algorithm (Leica Microsystems). 2. Either ImagJ or Matlab script were employed as described in Data collection and detailed in the Methods section 3.Maps of the instantaneous cellular velocities were obtained by analysing time-lapse movies and performing a PIV (Particle Image Velocimetry) analysis using the Matlab MPIV toolbox (http://www.oceanwave.jp/softwares/mpiv/ and https://www.mathworks.com/help/matlab/ref/curl.html) with the MQD (Minimum Quadric Differences) algorithm. 4. Statistic calculations were performed with GraphPad Prism 8 Software (https://www.graphpad.com/scientific-software/prism/). Data are expressed as mean ± SD, unless otherwise indicated. 5. image sequences obtained after analysis by ADAPT (OMICS_18880, Version 1.170) software that automatically tracks the dynamics of cell edges. Images were acquired every 90 sec over 3 h period.

For manuscripts utilizing custom algorithms or software that are central to the research but not yet described in published literature, software must be made available to editors/reviewers. We strongly encourage code deposition in a community repository (e.g. GitHub). See the Nature Research guidelines for submitting code & software for further information.

Data

Policy information about availability of data

All manuscripts must include a data availability statement. This statement should provide the following information, where applicable:

- Accession codes, unique identifiers, or web links for publicly available datasets
- A list of figures that have associated raw data
- A description of any restrictions on data availability

All Data are available on request from the authors

Field-specific reporting

Please select the one below that is the best fit for your research. If you are not sure, read the appropriate sections before making your selection.

☒ Life sciences ☐ Behavioural & social sciences ☐ Ecological, evolutionary & environmental sciences

For a reference copy of the document with all sections, see nature.com/documents/nr-reporting-summary-flat.pdf

Life sciences study design

All studies must disclose on these points even when the disclosure is negative.

Sample size	No predetermined samples was set. The number of experiments was determined based on previous pilot experiments and is indicated in each of the legend of the figures
Data exclusions	No data were excleded
Replication	Data were successfully replicated in at least 3 independent experiments
Randomization	This does not apply to the set of experiments prensented in this mansucript where two distinct groups were generally compared.
Blinding	The experiments were evaluated blindly by the operators

Reporting for specific materials, systems and methods

We require information from authors about some types of materials, experimental systems and methods used in many studies. Here, indicate whether each material, system or method listed is relevant to your study. If you are not sure if a list item applies to your research, read the appropriate section before selecting a response.

Materials & experimental systems

n/a	Involved in the study
☐	☒ Antibodies
☐	☒ Eukaryotic cell lines
☒	☐ Palaeontology
☒	☐ Animals and other organisms
☒	☐ Human research participants
☒	☐ Clinical data

Methods

n/a	Involved in the study
☒	☐ ChIP-seq
☒	☐ Flow cytometry
☒	☐ MRI-based neuroimaging

Antibodies

Antibodies used	Mouse monoclonal antibodies raised against α–tubulin (#T5168) or vinculin (#V9131) were from Sigma-Aldrich (dilution 1:400). Rabbit polyclonal anti-RAB5A (S-19, #sc-309) and goat polyclonal anti-EEA-1 (N-19, #sc-6415) antibodies from Santa Cruz

Biotechnology (Dilution 1:400). Monoclonal rabbit anti-human RAB5A - ab109534, dilution 1:100, (Abcam[EPR5438]) was used of IHC;Rabbit polyclonal anti-Giantin (#PRB-114C) antibody was from Covance. Mouse monoclonal anti-human Ki-67 Antigen (MIB-1, #M7240) antibody was from Dako (1:1000). Mouse monoclonal anti-AP50 (AP2mu) (31/AP50, #611350) was from BD Bioscience. Mouse monoclonal anti-E-cadherin (#610181) antibody was from Transduction Lab (Dilution 1:1000). Rabbit polyclonal anti-phospho-EGFR (Tyr1086, #2220), rabbit monoclonal anti-phospho-p44/42 MAPK (ERK1/2) (Thr202/Tyr204, #4370), rabbit polyclonal anti-p44/42 MAPK (ERK1/2) (#9102), rabbit monoclonal anti-phospho-p38 MAPK (Thr180/Tyr182, 3D7, #9215), mouse monoclonal anti-p38 MAPK (L53F8, #9228), rabbit monoclonal anti-phospho-AKT (Ser473, 193H12, #4058), rabbit polyclonal anti-AKT (#9272), rabbit polyclonal anti-MEK1/2 (#9122) and rabbit polyclonal anti-cleaved Caspase-3 (Asp175, #9661) antibodies were from Cell Signalling Technology (Dilution 1:1000). Rabbit polyclonal anti-phospho-WAVE2 (Ser343, #07-1512), rabbit polyclonal anti-phospho-WAVE2 (Ser351, #07-1514) and mouse monoclonal anti-Laminin-V (P3H9-2, #MAB1947) antibodies were from Merck/Millipore (Dilution 1:500). Mouse monoclonal anti-WAVE2 and mouse monoclonal anti-ABI1 antibodies were homemade54 (Dilution 1:100). Rabbit polyclonal anti-NAP1 antibody was a gift of Theresia Stradal (Helmholtz Centre for Infection Research, Braunschweig, Germany)55. Rabbit polyclonal anti EGFR (806), directed against aa 1172-1186 of human EGFR (ImmunoBlot) and mouse monoclonal anti-EGFR (m108 hybridoma) directed against the extracellular domain of human EGFR (IF) were a gift from P.P. Di Fiore (Dilution 1:1000). Secondary antibodies conjugated to horseradish peroxidase were all used at dilution 1:2000 and were from: Bio-Rad (#7074, #7076); Cy3-secondary antibodies from Jackson ImmunoResearch (#711-165-152, #715-165-150); DAPI (#D-1306) and AlexaFluor 488 (A-11055, A-21202) were from Thermo Fisher Scientific. TRITC- (#P1951) and FITC-(#P5282) conjugated phalloidin were from Sigma Aldrich.

Validation

All commercially available antibodies were validated for the use in westernblotting or immunoflurescence or immunohistopchemistry using siRNA or with purified proteins. Mouse monoclonal anti-WAVE2 and mouse monoclonal anti-ABI1 antibodies were homemade (1) (Dilution 1:100). Rabbit polyclonal anti-NAP1 antibody was a gift of Theresia Stradal (Helmholtz Centre for Infection Research, Braunschweig, Germany)(2). Rabbit polyclonal anti EGFR (806), directed against aa 1172-1186 of human EGFR (ImmunoBlot) and mouse monoclonal anti-EGFR (m108 hybridoma) directed against the extracellular domain of human EGFR (IF) were a gift from P.P. Di Fiore (Dilution 1:1000)(3).

1. Innocenti, M. et al. Abi1 regulates the activity of N-WASP and WAVE in distinct actin-based processes. Nat Cell Biol 7, 969-976 (2005).
2. Stradal, T.E. et al. Regulation of actin dynamics by WASP and WAVE family proteins. Trends Cell Biol 14, 303-311 (2004).
3. Sigismund, S. et al. Threshold-controlled ubiquitination of the EGFR directs receptor fate. The EMBO journal 32, 2140-2157 (2013).

Eukaryotic cell lines

Policy information about cell lines

Cell line source(s)

Cell line were obtained either from ATCC (HaCat). In the case of MCF10A cells they were a kind gift of J. S. Brugge (Department of Cell Biology, Harvard Medical School, Boston, USA) and were maintained in Dulbecco's Modified Eagle Medium: Nutrient Mixture F-12 (DMEM/F12) medium (Biowest) supplemented with 5% horse serum, 1% L-Glutamine (EuroClone), 0.5 mg ml−1hydrocortisone (Sigma-Aldrich), 100 ng ml−1 cholera toxin (Sigma-Aldrich), 10 µg ml−1 insulin (Sigma-Aldrich) and 20 ng ml−1 EGF (Vinci Biochem). MCF10.DCIS.com cells were kindly provided by J. F. Marshall (Barts Cancer Institute, Queen Mary University of London, UK) and maintained in Dulbecco's Modified Eagle Medium: Nutrient Mixture F-12 (DMEM/F12) medium supplemented with 5% horse serum, 1% L-Glutamine, 0.5 mg ml−1hydrocortisone, 10 µg ml−1 insulin and 20 ng ml−1 EGF. Phoenix-AMPHO (ATCC® CRL-3213™) were used as packaging cell line for the generation of retroviral particles and cultured as recommended by the supplier. HEK293T were obtained from BBCF-Biological Bank and Cell factory, INT, Milan grown in DMEM, 10% foetal Bovine serum, 2mM L-Glutamine and used as packaging line for lentiviral vectors.

Authentication

Each of the cell line is routinely tested for Mycoplasma and their identity verified by fingerprinting by our cell culture facility

Mycoplasma contamination

Each of the cell line is routinely tested for Mycoplasma and their identity verified by fingerprinting by our cell culture facility

Commonly misidentified lines
(See ICLAC register)

No commonly misidentified cell lines were used